Agricultural and Forest Meteorology 181 (2013) 69–84

Contents lists available at ScienceDirect

Agricultural and Forest Meteorology

journal homepage: www.elsevier.com/locate/agrformet

Long-term eddy covariance measurements of the isotopic composition of the ecosystem–atmosphere exchange of CO_2 in a temperate forest

R. Wehr[a,b,*], J.W. Munger[b], D.D. Nelson[c], J.B. McManus[c], M.S. Zahniser[c], S.C. Wofsy[b], S.R. Saleska[a,**]

[a] *Department of Ecology and Evolutionary Biology, University of Arizona, 1041 East Lowell Street, Tucson, AZ 85721, USA*
[b] *Department of Earth and Planetary Sciences, Harvard University, 20 Oxford Street, Cambridge, MA 02138, USA*
[c] *Aerodyne Research Inc., 45 Manning Road, Billerica, MA 01821, USA*

ARTICLE INFO

Article history:
Received 8 January 2013
Received in revised form 5 July 2013
Accepted 9 July 2013

Keywords:
Carbon dioxide
Isotope
Flux
Eddy covariance
Forest
Quantum cascade laser spectrometer

ABSTRACT

Measurements of the isotopic composition of the net ecosystem–atmosphere exchange of CO_2 (NEE) have been desired as a means to probe ecosystem carbon cycling and in particular to partition NEE into gross ecosystem photosynthesis and respiration. Several attempts at such measurements have combined eddy covariance (EC) measurements of the total net CO_2 flux with flask measurements of the isotopic composition of CO_2 in ambient air – an indirect method that has never been validated. Direct EC measurements of the isotopic composition of NEE (i.e. of the net exchanges of $^{12}C^{16}O_2$, $^{13}C^{16}O_2$, and $^{18}O^{12}C^{16}O$) have been made only twice, in short-term (2-month and 1-month) campaigns.

Here we present a full growing season of direct EC measurements of the isotopic composition of NEE in a temperate deciduous forest, and we use these data: (1) to rigorously assess their limiting sources of error, (2) to test the indirect EC/flask method, and (3) to give an indication of the potential for ecological analyses. We describe the method and instrumentation, including the new cryogen-free, continuous-wave, quantum cascade laser spectrometer, which can determine $\delta^{13}C$ and $\delta^{18}O$ in ambient CO_2 with unprecedented noise levels of ±0.02‰ and ±0.03‰ (1 standard deviation), respectively, for a 100 s integration time and a 1-h calibration interval. We find: (1) that precision is jointly limited by the instrumentation and by horizontal ecosystem or landscape heterogeneity, so that there is little to be gained by further improvements to instrument performance; (2) that the isotopic composition of NEE obtained by the EC/flask method can be biased, on a monthly timescale, by 2‰; and (3) that the present measurements are precise enough to elucidate biological mechanisms controlling the ecosystem-scale carbon balance.

1. Introduction

The stable isotopic composition of the net ecosystem–atmosphere exchange (NEE) of CO_2 carries information about the mechanisms of ecosystem carbon cycling. Processes such as carboxylation, diffusion, and dissolution of CO_2 in water fractionate the isotopologues of CO_2 (Farquhar et al., 1993, 1989). The isotopic composition of the net CO_2 exchange could therefore be used to probe these processes, and provides an independent constraint for evaluating biophysical ecosystem models. It could also clarify the influence of ecosystems on the isotopic budget of the atmosphere, which has ramifications for land/sea, source/sink partitioning (Yakir and Sternberg, 2000). Moreover, it could be used to partition NEE into gross primary productivity and gross ecosystem respiration (Bowling et al., 2001; Knohl and Buchmann, 2005; Ogée et al., 2003; Saleska et al., 2006; Zobitz et al., 2008).

Until recently, however, the isotopic composition of NEE was not strictly measurable. NEE is normally and most directly measured by the eddy covariance (EC) method, with the CO_2 molar mixing ratio above the canopy provided by a non-dispersive infrared gas analyzer (IRGA). To measure the isotopic composition of NEE by EC, one must replace the IRGA with an isotopic CO_2 monitor capable of resolving the eddy-induced isotopic fluctuations above

---

[*] Corresponding author at: Department of Earth and Planetary Sciences, Harvard University, 20 Oxford Street, Cambridge, MA 02138, USA. Tel.: +1 781 300 1976.
[**] Corresponding author at: Department of Ecology and Evolutionary Biology, University of Arizona, 1041 East Lowell Street, Tucson, AZ 85721, USA. Tel.: +1 520 626 1500.

E-mail addresses: rawehr@arizona.edu, richardwehr@fas.harvard.edu (R. Wehr), jwmunger@seas.harvard.edu (J.W. Munger), ddn@aerodyne.com (D.D. Nelson), mcmanus@aerodyne.com (J.B. McManus), mz@aerodyne.com (M.S. Zahniser), swofsy@seas.harvard.edu (S.C. Wofsy), saleska@arizona.edu (S.R. Saleska).

0168-1923/$ – see front matter © 2013 Elsevier B.V. All rights reserved.
http://dx.doi.org/10.1016/j.agrformet.2013.07.002

the ecosystem over all timescales at which significant fluctuations occur. Above a forest canopy, significant fluctuations in δ^{13}C occur over timescales from 1 s to 30 min, with a typical standard deviation of just 0.02‰ (Saleska et al., 2006), and no capable CO$_2$ isotope monitor existed until the development of a specialized quantum cascade laser spectrometer (QCLS) in 2008 (Nelson et al., 2008; Tuzson et al., 2008).

In the absence of direct isotopic flux measurements, several studies aimed at partitioning NEE (Bowling et al., 2001, 1999; Knohl and Buchmann, 2005; Lai et al., 2003; Ogée et al., 2003, 2004; Zobitz et al., 2008, 2007) have used what is called the EC/flask method (Bowling et al., 1999) to determine the carbon isotopic composition of NEE indirectly. The EC/flask method employs flask samples of canopy or above-canopy air (transported to a laboratory for analysis by isotope ratio mass spectrometry, or IRMS) to establish a simple functional relationship between δ^{13}C and the total CO$_2$ molar mixing ratio *C*. Given such a relationship, the carbon isotopic composition of NEE can be easily calculated. However, changes in the relative contributions of respiration and photosynthesis to the net flux (i.e. precisely those changes of interest to flux partitioning), as well as changes in the photosynthetic fractionation, ensure that no such relationship is exact on a diel timescale. The EC/flask method is therefore inherently approximate, and a test of the accuracy of the approximation is needed.

The first set of direct EC measurements of the isotopic composition of NEE was acquired using a lead salt diode laser spectrometer (predating QCLSs) in a soybean field over a period of 2 months (Griffis et al., 2008), but the measurement noise in the δ^{13}C and δ^{18}O of ambient CO$_2$ was about ±0.25‰ for an integration time of 4.5 min, which is insufficient to assess isotopic exchange in critically important forest ecosystems. The only other set of direct isotopic flux measurements (Sturm et al., 2012) was acquired using a QCLS in a deciduous forest over a period of one month. There the measurement noise in δ^{13}C and δ^{18}O was about ±0.05‰ for an integration time of 100 s, but the spectrometer required cryogenic cooling, restricting its long-term and remote use.

Here we describe an improved QCLS design, which we have used to produce the first long-term (whole growing season) record of ecosystem–atmosphere CO$_2$ isotopologue exchange, measured by EC at the Harvard Forest, a temperate deciduous forest in central Massachusetts. The improved design is cryogen-free, uses a continuous-wave laser, measures the isotopic composition of CO$_2$ in ambient air with uncertainties of ±0.02‰ (δ^{13}C) and ±0.03‰ (δ^{18}O) for a 100 s integration time, and requires calibration only hourly. We use our isotopic flux record, first, to test the EC/flask method, by comparing our results to those that would have been obtained from our data by that method. Second, we assess the sources of uncertainty that remain in state-of-the-art EC measurements of isotopic CO$_2$ exchange, including an examination of the report in Sturm et al. (2012) that random error associated with EC data processing is limiting. Third, we offer some preliminary examples of how our results can elucidate ecosystem carbon dynamics, and we consider the potential for partitioning NEE into gross photosynthesis and respiration. In a follow-up paper, we will directly test this instrument's capability for partitioning.

2. Theory

In this section, we review the theoretical framework for the analysis of field measurements. We use the following notation. Two-digit superscripts denote (intramolecular) atoms according to the mass of the intended isotope: "13" for ^{13}C, "18" for ^{18}O, etc. Isotopic compositions are expressed in standard δ notation, i.e. δ^{18}O is the relative deviation of the isotope ratio $R^{18} = {}^{18}\text{O}/{}^{16}\text{O}$ from that ratio in a standard material. We use the Vienna Pee Dee Belemnite (VPDB) standard for ^{13}C and the Vienna Standard Mean Ocean Water (VSMOW) standard for ^{18}O, with $R^{13}_{\text{VPDB}} = 0.0111797$ (Griffis et al., 2004) and $R^{18}_{\text{VSMOW}} = 0.0020052$ (Baertschi, 1976; Allison et al., 1995). We abbreviate δ^{13}C and δ^{18}O as δ^{13} and δ^{18} (note the italics) when convenient.

Assuming horizontal homogeneity, the net ecosystem exchange of CO$_2$ (NEE or F_N, μmol m^{-2} s^{-1}) can be written as

$$F_N = F_E + F_S \tag{1}$$

where the eddy flux F_E and the storage flux F_S are defined as

$$F_E \equiv \overline{c_d} \cdot \overline{w'C'} \tag{2}$$

$$F_S \equiv \int_0^h c_d(z)\frac{dC(z)}{dt}dz \approx \overline{c_d}\frac{d}{dt}\int_0^h C(z)dz \tag{3}$$

where in turn t is time (s), z is height (m), c_d is the concentration of dry air (mol m^{-3}), $C = c/c_d$ is the molar mixing ratio of CO$_2$ to dry air (μmol mol^{-1}), overbars denote time averaging over the EC integration period (30 min here), and primes denote deviations from the corresponding EC integration period means, as per Reynolds decomposition ($a \equiv \bar{a} + a'$). This result can be obtained from Eq. (6.13) of Lee et al. (2004) by assuming horizontal homogeneity and dropping what they call the vertical advection term, which we found to be −0.001 ± 0.012 μmol m^{-2} s^{-1} across the set of flux measurements presented here. Note that F_E and F_S are the net eddy and storage fluxes associated with production or consumption of CO$_2$ below $z = h$, i.e. they exclude the net eddy and storage fluxes of CO$_2$ associated with the redistribution of dry air as a whole, which are not negligible but which balance one another (Leuning, 2007) and are irrelevant for ecological studies.

Equations analogous to Eqs. (1)–(3) can be written for any individual CO$_2$ isotopologue, or for any intramolecular isotope of C or O. Moreover, if one replaces C with the product $\delta^{13} \cdot C$, then the fluxes become ^{13}C isofluxes (‰ μmol m^{-2} s^{-1}): the net isoflux I^{13}_N, the eddy isoflux I^{13}_E, and the storage isoflux I^{13}_S. The same applies to ^{18}O.

The ^{13}C and ^{18}O isotopic compositions of NEE are defined as:

$$\delta^{13}_N \equiv \frac{(F^{13}_N/F^{12}_N)}{R^{13}_{\text{VPDB}}} - 1; \quad \delta^{18}_N \equiv \frac{(F^{18}_N/F^{16}_N)}{R^{18}_{\text{VSMOW}}} - 1. \tag{4}$$

To a very good approximation (i.e. aside from isotope clumping effects), the carbon isotope ratio ^{13}C/^{12}C is equal to the isotopologue ratio ^{13}CO$_2$/^{12}CO$_2$ while the oxygen isotope ratio ^{18}O/^{16}O is equal to half the isotopologue ratio ^{18}O^{12}C^{16}O/^{16}O^{12}C^{16}O, and the same holds true for the corresponding fluxes (see Appendix for more details). Using the definitions in Eqs. (4), one can write the isofluxes as $I^{13}_N = \delta^{13}_N F_N$ and $I^{18}_N = \delta^{18}_N F_N$.

3. Methods

3.1. Site

The data presented here were collected from May to October 2011 at the Harvard Forest Environmental Measurements Site (HF-EMS) in Petersham, Massachusetts, USA. Continuous measurement of NEE, latent and sensible heat flux, and associated meteorological variables began at HF-EMS in 1989, making it the longest-running eddy covariance measurement site in the world. The site is located in a temperate deciduous forest dominated by red oak and red maple, and has been described in detail previously (Goulden et al., 1996; Barford et al., 2001; Urbanski et al., 2007; Wofsy et al., 1993).

The QCLS for real-time isotopic CO$_2$ measurements was added to the existing instrument shack, about 10 m from the base of the eddy flux tower, and dedicated ¼″ (outside diameter) air sampling

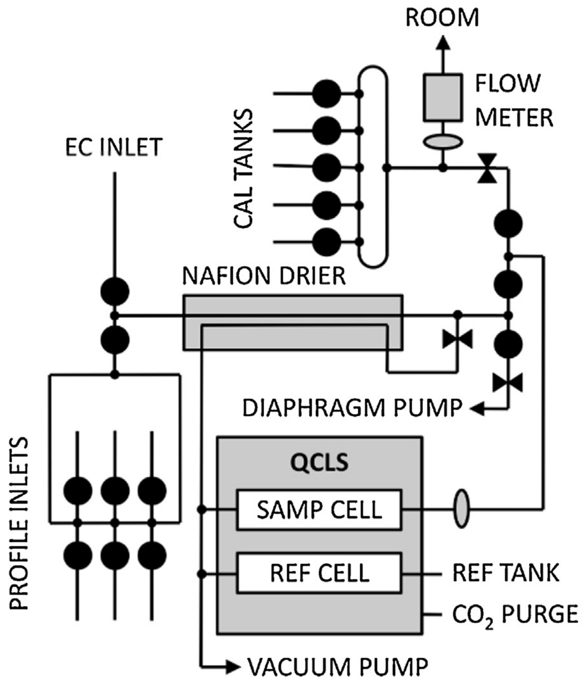

Fig. 1. Schematic diagram of the gas flow system. Solenoid valves are shown as black circles, fixed flow restrictions as paired triangles, and low-volume 2 μm air filters as gray ovals.

tubing (Eaton Synflex 1300) was strung up the tower. Seven lines were added, including the main "EC" line with its inlet at a height of 29 m (on the same boom as the existing Applied Technologies Inc. sonic anemometer and CO_2 sampling inlet) and 6 "profile" lines with their inlets at 0.2, 1, 7.5, 12.7, 18.3 and 24.1 m.

Gaps in the HF-EMS meteorological record were filled with data from Fisher Meteorological Station, about 1.5 km to the southwest, also within the Harvard Forest.

3.2. *Sampling*

The 7 tower inlet lines and 5 calibration cylinder lines were connected to a custom-built valve manifold, which was used to select which line the spectrometer would sample from. This manifold consisted of a datalogger (Campbell CR800) and relay controller (Campbell SDM-CD16S), which controlled 16 solenoid valves (Entegris Galtek PFA diaphragm valves with ¼″ orifices, model 203-1414-115) in the arrangement depicted in Fig. 1. This arrangement was chosen to minimize dead volume and mixing volume, especially when the EC line was selected, as dead or mixing volume would act to smear out the high-frequency information in the air stream and reduce the measured eddy flux. During normal operation, the manifold was programmed to follow a 40-min duty cycle containing 30 min for the EC inlet, 2 min for each of two calibration cylinders (see Section 3.5), and 1 min for each of the 6 profile inlets. The spectrometer's vacuum pump (Varian TriScroll 600) pulled 4 standard liters per minute (slpm) through the selected line. The tube transit time for the EC inlet was just under 10 s; the profile lines were shorter.

A 2 μm Teflon filter in a 47 mm diameter holder was put inline shortly after the inlet for each profile line, to prevent particles from reaching the spectrometer. For the EC line, an open-faced filter holder made by cutting the end off an inline holder was used so there would not be a mixing volume in the line. All the sample lines then fed (after selection by the manifold) into a Nafion drier (Perma Pure PD-200T-48) specified to lower the dew point below −32 °C (i.e. 300 ppm water vapor by volume). The goal of the drier was to reduce the water vapor content of the air stream to a point where dilution of CO_2 by water vapor in the spectrometer's sample cell (and resulting error in the CO_2 dry-air molar mixing ratio measurement) would be negligible. The effectiveness of the drier was tested by sending dry cylinder air alternately through a bubbler and not, before the spectrometer, and checking for any change in the measured CO_2 molar mixing ratio. None was detected, although errors in the total ambient CO_2 molar mixing ratio as large as 0.1 ppm might be expected based on the drier's specifications.

The time response of the system (including the ~50 m of Synflex tubing and the 48″ long, 200-tube Nafion drier) was tested in the lab at a flow rate of 5 slpm by observing the instrument response to a CO_2 molar mixing ratio square wave created by switching back and forth between two cylinders of different molar mixing ratios. The drier was the limiting element to the response time. The 10–90% rise time of the total system was 0.5 s, compared to 0.25 s without the drier, and 0.15 s just to flush the spectrometer's sample cell. We calculated theoretical tube flow conditions for this test based on Lenschow and Raupach (1991). The Reynolds number was about 1700, which is somewhat in the laminar flow regime (<2300). However, the laminar transfer function for the test conditions predicts that only 1% of a 2 Hz signal should survive the tubing, whereas the turbulent transfer function predicts that 75% should survive. The experimental value of 80% (corresponding to the 10–90% rise time of 0.25 s without the drier) suggests either that the tube flow was actually turbulent or that coiling of the tubing worked to homogenize the radial velocity profile and so reduce signal smearing, as discussed in Lenschow and Raupach (1991). This test was performed with a single small-orifice, 3-way switching valve, not the large-orifice, 16-valve manifold used in the final field configuration. The flow rate was also 1 slpm higher than in the final field configuration, and the tubing was coiled rather than (roughly) straight. Thus some additional signal attenuation should be expected in the field measurements (see Section 3.6). Moreover, the ~0.5 m horizontal separation of the CO_2 inlet from the sonic anemometer should contribute some additional high-frequency signal attenuation in the field.

One potential concern in the sampling system, specifically for the $^{18}O^{12}C^{16}O$ measurements, was water condensation in the tower tubing, particularly on hot days where the tubing enters the air-conditioned (22 °C) instrument shack. The pressure drop along the tower tubing (~10 kPa) reduced the dew point where the tubing enters the shack by about 2 °C, so that condensation could be expected only when the ambient dew point reached 24 °C – a situation that occurred during only 1% of the measurement duty cycles in 2011. We therefore do not expect condensation to have significantly affected our results. Moreover, the air speed in the sample lines within the instrument room was roughly 5 m/s, and so the time available for CO_2 to interact with condensed water was only a fraction of a second, which is not long enough for significant CO_2 or ^{18}O exchange.[1]

3.3. *Spectrometer design*

Here we briefly describe the improved QCLS design, noting differences from the original design reported in Nelson et al. (2008).

---

[1] Consider that when complete $\delta^{18}O$ equilibration is desired in the preparation of samples for IRMS analysis, it is recommended that the CO_2 and H_2O be *shaken* together (to encourage dissolution) for 4–8 h (Mook, 2000). Assuming that "complete" means 99.999% and that exchange is an exponential decay process, the implied rate constant is at most 0.0008 s^{-1}, which means that even if we imagined dissolution and hydration to occur as readily in our tube as in a shaken vial, only 0.3 out of 400 ppm CO_2 would be isotopically equilibrated with H_2O in a 5 m segment of thoroughly wet tube. The real number must be much lower.

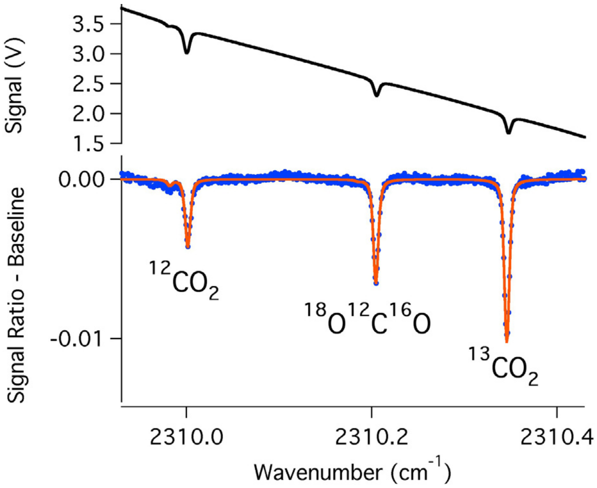

Fig. 2. Example QCLS spectra. The top panel shows the infrared signal measured through the reference cell (containing roughly 400 ppm CO_2 in air) in 0.25 s, where zero volts would indicate no transmitted light. The bottom panel shows the measured sample cell spectrum (blue) after division by the measured reference cell spectrum and subtraction of a 3rd order polynomial baseline; also shown is the theoretical fit (orange) used to retrieve the CO_2 isotopologue concentrations. (For interpretation of the references to color in this figure legend, the reader is referred to the web version of this article.)

The key differences between the current spectrometer and that of Nelson et al. (2008) and Tuzson et al. (2008) are: (1) a continuous-wave QCL in place of a pulsed QCL, and (2) thermo-electrically (TE) cooled HgCdTe detectors (Teledyne Judson Technologies) in place of liquid nitrogen-cooled InSb detectors. The instrument is therefore cryogen-free. In addition, we do not employ the dilution calibration method described in Nelson et al. (2008), having found that independent linear calibration of each isotopologue molar mixing ratio between two standard cylinders that bracket the measured molar mixing ratios is both simpler and more accurate for this instrument (see Section 3.5).

The spectrometer operates by repeatedly tuning its laser across the spectral region 2309.9–2310.6 cm^{-1} and measuring the absorption of the laser beam by CO_2. A sample absorption spectrum is shown in the top panel of Fig. 2. This spectral region is unique in that it includes three well-spaced absorption lines of roughly equal optical depth, each associated with a different CO_2 isotopologue. There are also numerous weaker lines, only two of which are strong enough to merit inclusion in the spectral analysis: a $^{17}O^{12}C^{16}O$ line in the shoulder of the main $^{12}C^{16}O_2$ line, and a very weak $^{12}C^{16}O_2$ line in the shoulder of the $^{18}O^{12}C^{16}O$ line. The concentration of $^{17}O^{12}C^{16}O$ is fixed relative to $^{12}C^{16}O_2$ using their natural abundances when fitting the spectra – a good approximation in this context.

The laser beam is split in two, and each branch passes though a multi-pass optical cell with an optical path length of 7.44 m and a volume of 0.3 L. The sample air stream flows through one cell (the sample cell) at a rate of 4 slpm and a pressure of 20.0 torr (2.67 kPa). Air from a cylinder of CO_2 in air (with a CO_2 molar mixing ratio fixed at various values between 320 and 450 ppm over the course of the present study) flows through the other cell (the reference cell) at a rate of 0.05 slpm and also at a pressure of 20.0 torr. The flow through both cells is pulled by the same vacuum pump (Varian TriScroll 600). The molar mixing ratio of the reference cell gas does not have to be known accurately, as it does not affect the retrieved sample gas molar mixing ratio after calibration; however, the closer the reference gas molar mixing ratio is to the sample gas molar mixing ratio, the lower the short-term instrument noise (see Section 4.1).

The spectra are acquired at a rate of 900 Hz and averaged down to 4 Hz to improve the signal-to-noise ratio. The 4 Hz sample cell spectra are then divided by the 4 Hz reference cell spectra before further analysis, in order to shrink the spectral lines and thereby reduce the noise caused by laser frequency instability. The resulting noise reduction varies between 3× and 10× depending on the electrical environment of the instrument. The divided spectrum is fitted for each isotopologue molar mixing ratio using Voigt profiles with fixed line positions, intensities, and broadening coefficients from the HITRAN database (Rothman et al., 2009) and using the measured temperatures and pressures of the cells (which must be closely matched and stabilized for optimal short-term precision). A third-order polynomial baseline is incorporated into the fit. An example spectrum after division and baseline subtraction is shown in the lower panel of Fig. 2, where one can see that the line-peak fractional absorption of roughly 10% in the top panel has been effectively reduced to less than 1% by dividing the two cell signals. This spectrum was recorded in the early morning, when CO_2 levels above the forest were still elevated from the accumulation of respired CO_2 through the night.

The total CO_2 molar mixing ratio and the isotope ratios must be calculated from the individual isotopologue molar mixing ratios measured by the spectrometer. This calculation requires some assumptions about the molar mixing ratio of $^{12}C^{17}O^{16}O$ and other unmeasured isotopologues, although the results are not significantly affected by the uncertainties associated with these assumptions. For the details of our procedure, see Appendix.

3.4. Spectrometer stability improvements

After initial testing, we made five key improvements to the spectrometer in order to improve its stability, which was limited by several concurrent sensitivities to room temperature. These sensitivities were exacerbated by strong temperature cycles in the HF-EMS shack (a 2 °C drop in 2 min, on a 10- to 30-min cycle) associated with a densely packed instrument room cooled by a single air conditioner. We briefly summarize the stability issues here for the benefit of users of similar instruments. Our experience is that careful thermal management of internal (and some external) components is crucial to the performance of most, if not all, high-precision laser spectrometers.

i. *Detector heterogeneity*. We replaced the first set of TE-cooled detectors (Vigo System S.A.) with Teledyne Judson HgCdTe TE-cooled detectors. The first set incorporated high-index immersion lenses to couple the laser light into small detector elements, and the overall response function was heterogeneous across the face of the detector. The reported molar mixing ratios were therefore ultra-sensitive to the subtle alignment changes that accompany microscopic thermal expansion and contraction of the optical box – even with the temperature at two thermistor locations within the optical box controlled to within 50 mK. Switching to the Teledyne Judson detectors when they became available effectively eliminated this problem.
ii. *Optical box isolation*. We added insulation with an *R*-value of 1.76 $m^2\,K\,W^{-1}$ around the optical box, further reducing the alignment perturbations caused by thermal expansion and contraction. We also improved the optical box air seals in order to reduce (from 1 to 0.2 L/min) the gas flow used to purge it of CO_2. Finally we added thermal preconditioning to both the purge flow and the sample gas flow by passing each gas through about 2 m of ¼″ copper tubing woven into a heated aluminum block.
iii. *Cell temperature differential*. We modified the instrument software to use the sample cell thermistor reading for both (sample and reference) cells. We had found that offsets in the thermistors recording the sample and reference cell temperatures

were larger than the actual cell temperature differences, and introduced error into the molar mixing ratios. Ignoring the thermistor disparity improved the stability of the mixing ratio measurements.

iv. *Synflex tube wall interaction*. We added thermal insulation to the Synflex tubing between the reference gas cylinder and the spectrometer. The reference cell gas flow rate was under 0.05 slpm, and it passed through 4 m of ¼″ Synflex tubing on its way from the cylinder pressure regulator to the instrument. We found that fluctuations in the temperature of this tubing were inducing variations in the real molar mixing ratio emerging from the tubing, at the level of roughly 0.1 ppm/K. Switching the tubing to 1/8″ PTFE increased the sensitivity to 0.5 ppm/K, and switching the tubing to 1/8″ stainless steel of unknown history (presumed to have residue on the inner walls) increased the sensitivity even further, to 5 ppm/K. Simply adding thermal insulation to the original Synflex tubing eliminated the sensitivity (or reduced it to immeasurable levels). We hypothesize that CO_2 is adsorbed on the interior surface (and/or pores) of the Synflex (and other) tubing in a temperature-dependent way, such that when the temperature of the tubing increases, CO_2 leaves the tubing wall and raises the molar mixing ratio of the gas stream temporarily. This effect was not observable at the higher flow rate (4 slpm) used in the sample cell. Whether the effect might be eliminated by using thoroughly cleaned stainless steel tubing has not yet been investigated, as insulating the Synflex tubing was a simpler and sufficient solution for the purposes of this study.

v. *Laser current drift*. We enclosed the instrument electronics in a thermally regulated box – using a Custom Chill recirculating water cooler, a tube-fin heat exchanger with fan, and foam insulation with an *R*-value of $1.76\,m^2\,K\,W^{-1}$. Once the effect of the Synflex tube wall interaction had been eliminated, we were able to determine that the instrument electronics were sensitive to the temperature of the room air used for cooling them. In particular, the laser driver (ILX Lightwave 3232) seemed to be the problematic element. The current supplied by the driver to the laser varied with room temperature, and the instrument in turn adjusted the laser temperature to maintain the same infrared frequency. The combination of the current change and the temperature change altered the laser output power as well as its tuning rate. The tuning rate change stretched the spectrum, causing the line center frequencies of the measured $^{12}CO_2$ and $^{13}CO_2$ lines to be shifted relative to where the analysis software expected them to be. The molar mixing ratio of the $^{18}O^{12}C^{16}O$ line in the middle of the scan was unaffected, as the position of this line was constantly measured and used to maintain a constant spectral window for the scan. Thermal regulation of the laser driver and other electronics effectively eliminated this problem.

3.5. Calibration

Laser absorption spectrometers do not measure $\delta^{13}C$, $\delta^{18}O$, or *C* directly. Instead they measure the concentration ($mol\,m^{-3}$) of each isotopologue. Those concentrations (which are converted to molar mixing ratios using the measured temperature and pressure) are therefore the quantities we wish to calibrate, before using them in calculations of δ and *C*. In principle, it is possible for an instrument to suffer from cross talk between the isotopologue absorption features, so that the retrieved molar mixing ratio of, say, $^{13}CO_2$ depends on the amount of $^{12}CO_2$ or $^{18}O^{12}C^{16}O$ in the sample; however, we did not find cross talk in our instrument. On the contrary, we found that a plot of measured versus true molar mixing ratio for any given isotopologue was highly linear (for repeated validations in the field (see Section 4.2 and Fig. 5).[2] We were therefore able to calibrate the retrieved isotopologue molar mixing ratios independently, using just two "working tanks": a high span gas cylinder with roughly 450 ppm CO_2 in air, and a low span cylinder with roughly 350 ppm CO_2 in air. These tanks bracketed the sample gas *C* except when sampling from the subcanopy at night (when *C* can reach 650 ppm). Systematic extrapolation errors in the 0.2 m and 1 m tower profile measurements are therefore a possibility; however, such errors are not likely to be larger than twice our usual systematic instrument errors, which are negligible in the context of our tower profile analyses (i.e. canopy storage measurements and Keeling plot analyses). Note that it is not necessary for the working tanks to bracket the sample gas isotope ratios, as the variation in those ratios is small enough (always less than a few percent) that any two cylinders bracketing *C* also bracket the individual isotopologue molar mixing ratios.

Table 1
Short-term instrument noise for *C* (top value), $\delta^{13}C$ (middle value), and $\delta^{18}O$ (bottom value), for different integration times and sample-reference gas mixing ratio disparities.

		Integration time (s)	
		0.25	100
$C_{sam} - C_{ref}$ (ppm)	0	57 ppb	16 ppb
		0.2‰	0.02‰
		0.2‰	0.03‰
	100	85 ppb	16 ppb
		0.4‰	0.02‰
		0.4‰	0.03‰

The working tanks were sampled for 2 min each, one after the other, once every 40-min duty cycle, but data from the first 30 s of each 2-min measurement were discarded to avoid transients during cell flushing. The slopes and intercepts of the resulting calibration lines were interpolated onto the 4 Hz sample times and used to calibrate each sample measurement. This approach is more accurate than relying only on the previous standard measurement, but necessitates that calibration be done in post-processing rather than in real time.

Each pair of working tanks was calibrated in turn against three primary standard cylinders (at 332.69(6) ppm, 431.15(6) ppm, and 496.49(6) ppm CO_2 in air) when the working tanks were full (~2000 psi) and when they had ~500 psi remaining, after which the working tanks were replaced to avoid the possibility of variations in *C*, $\delta^{13}C$, or $\delta^{18}O$ as the cylinders neared depletion. Before deployment, the primary standards were characterized by IRMS at the Stable Isotope Ratio Facility for Environmental Research at the University of Utah (for the isotope ratios) and by an IRGA (calibrated with a set of primary CO_2 standards obtained from NOAA-GMD) in the Wofsy/Munger Laboratory at Harvard University (for the CO_2 molar mixing ratio). Calibration of the working tanks against the primary standards was done using the spectrometer itself, in the field – an approach justified by the fact that the spectrometer's short-term precision (see Table 1 and Section 4.1) and long-term repeatability (69 ppb for *C*, 0.05‰ for $\delta^{13}C$, and 0.06‰ for $\delta^{18}O$ over 6 months; see Section 4.2) are comparable to or better than the reported uncertainties of the IRMS- and IRGA-based techniques used to calibrate our primary standards (60 ppb for *C*, 0.06‰ for $\delta^{13}C$, 0.22‰ for $\delta^{18}O$).

---

[2] Although the measured molar mixing ratio of a given isotopologue does not depend on the amount of any other isotopologue in the sample, the three isotopologue measurements do share some common noise sources (e.g. laser frequency instability), so that their random measurement errors are partly correlated. The noise correlation is strongest at high frequency (the correlation coefficient can be around 0.7 at 4 Hz) and becomes negligible with averaging to 90 s.

3.6. Flux calculations

The eddy flux calculations began with rotating the sonic anemometer wind velocities into natural wind coordinates (Lee et al., 2004) using double rotation rather than triple rotation, in order to avoid the problem of over-rotation. We then linearly interpolated the vertical wind and air temperature (both recorded by the sonic anemometer at 10 Hz) and the CO_2 data (recorded by the spectrometer at 4 Hz) onto a time grid containing 2^{15} points in preparation for multiresolution decomposition (MRD) (Howell and Mahrt, 1997). MRD requires 2^M points, for any positive integer M (see below). A 30-min flux averaging period divided into 2^{15} points yields a time step of 0.055 s. Next, we determined the precise time lag between the anemometer data and the spectrometer data (due to tube lag, sensor separation, and clock offsets) by scanning the CO_2 time series across the vertical wind time series in 0.055 s steps and finding the lag for which the covariance was maximized.

Finally, MRD was used to compute the "multiresolution cospectrum", i.e. to compute the eddy covariance for M different averaging periods corresponding to 2^1, 2^2,. . .,2^M points. Block averaging is implicit in MRD and so it was not necessary to block average beforehand. The simple sum of all M terms in a multiresolution cospectrum gives the total eddy covariance. MRD gives the same covariance as does the ordinary calculation, but produces its multiresolution cospectra (MRCs) in the process. These cospectra are argued to be superior to Fourier cospectra for turbulent flux analysis because the multiresolution cospectra are sensitive to the scale of the turbulent eddies whereas Fourier cospectra, being sensitive to periodicity, are biased to longer timescales by the intermittent nature of those eddies (Howell and Mahrt, 1997). In any case, multiresolution cospectra facilitate our spectral correction for high-frequency CO_2 signal loss, described in Section 4.3.

We add a final technical detail. Before the above-described eddy flux calculations were performed, we had to synchronize the anemometer and spectrometer data. This synchronization was non-trivial because the anemometer data was logged by the existing non-isotopic EC system, which recorded all its data in a self-consistent telemetry frame, but whose telemetry timestamp generated by software was independent of its system clock. The telemetry timestamp drifted away from the system clock at a constant rate of ~30 s per day but was reset at the start of each data file (usually every 12 h) as well as at irregular times during some files if they were interrupted and restarted for any reason (helpfully marked by rows of zeros). Thus, although both system clocks were regularly synchronized to NIST, the relative error between the anemometer and spectrometer timestamps varied as a quasi-periodic, sawtooth-like function. We developed an algorithm in Igor (Wavemetrics Inc.) that recognized and fit, with a series of straight lines, the linearly drifting and sporadically resetting timestamp error over time, based on a relatively quick comparison of low-resolution (0.25 s) temperature and C time series across a wide range of lags. (Using the sonic anemometer's temperature time series was more reliable than using the vertical wind speed.) This method was robust despite fairly common periods when the covariance was too small for an accurate lag determination. Based on the timestamp error retrieved by this algorithm, the sonic anemometer files were stitched together or cut apart as appropriate, and then their time stamps were shifted and stretched to match the spectrometer time series. The full covariance code was then run, including the precise lag determination mentioned above.

3.7. EC/flask simulation

There are several variations on the EC/flask method. Knohl and Buchmann (2005) used flask samples from within- and above-canopy heights (2–40 m), and fit the linear relation $\delta = mC + b$ to their data. Heights below 2 m were excluded to avoid a bias toward soil respiration. Bowling et al. (2001) restricted their flask samples to two above-canopy heights (26 and 37 m) and fit the same relation. Ogée et al. (2003) restricted their flask samples to their eddy covariance measurement height (25 m) and fit the relation $\delta C = mC + b$ (equivalent to the Keeling relation $\delta = b/C + m$). All studies restricted their flask samples to daylight hours (nighttime flasks were collected, but for other purposes).

We have chosen to simulate the EC/flask method as implemented in Knohl and Buchmann (2005) because the other implementations were restricted to above-canopy flask measurements around midday, which would lack sufficient range in C for useful regressions at our site. Broadening the C range by using samples collected toward dawn or dusk would be problematic as any approximate relationship between δ and C breaks down over times longer than a few hours (as it must in order for the isotopic composition of NEE to shift from its daytime, photosynthesis-dominated value to its nighttime respiration value). We did not collect actual flasks but instead treated the average of each of our 1-min tower profile measurements as if it were a flask measurement. As in Knohl and Buchmann (2005), we excluded heights below 2 m and considered samples only around noon (11 am–1 pm). We fit the relation $\delta = mC + b$ to our simulated flask measurements, separately for each day, and interpolated the coefficients m and b in time. The isotopic composition of the eddy flux (not NEE) was then computed for each duty cycle as $\delta_E^{13} = 2m\bar{C} + b$, where $\bar{C}$ is the mean value of C over the 30-min EC measurement. This formula follows from inserting the relation $\delta = mC + b$ into the definition of eddy isoflux (see Section 2), as shown in Bowling et al. (2001).

To obtain the isotopic composition of NEE, one would first compute the isoflux as the sum of the eddy isoflux, $I_E^{13} = (2m\bar{C} + b)F_E$, and the storage isoflux, the latter of which would have to be obtained from flask samples taken at various heights in the canopy and subcanopy before and after each eddy flux integration period. One would then divide the isoflux by NEE to obtain δ_N^{13}. We do not bother to compute δ_N^{13} by the EC/flask method, as it is more straightforward to compare the EC/flask and EC methods in terms of the isotopic composition of the eddy flux (Section 4.5); the storage flux (and storage isoflux) would be identical for both methods in a flask simulation such as ours.

Note that the EC/flask method is not even approximately valid for $\delta^{18}O$ (Bowling et al., 1999).

4. Results and discussion

As with standard EC systems, "lost flux" was observed on calm nights and might also play some role during other periods. Data used for the analyses presented here were therefore filtered to exclude times when $u^* < 0.17$ m/s (Urbanski et al., 2007).

4.1. Short-term instrument noise and stability

In this article, we use the most general definitions of signal and noise: *signal* means the pattern of variation that we wish to measure in a quantity like w or C, and *noise* means all other variation in that quantity, which interferes with our ability to discern the signal. Noise in general therefore includes all measurement noise (e.g. short-term instrument noise and instrument drift) as well as natural noise, i.e. any variation in the real quantity that is unrelated to what we are trying to see. In this section, however, we consider only short-term (<3 h) instrument noise.

We quantify instrument noise by the standard deviation σ_m of repeated measurements of a constant input (such as gas from a cylinder). This deviation is inversely related to the precision and depends on the following parameters.

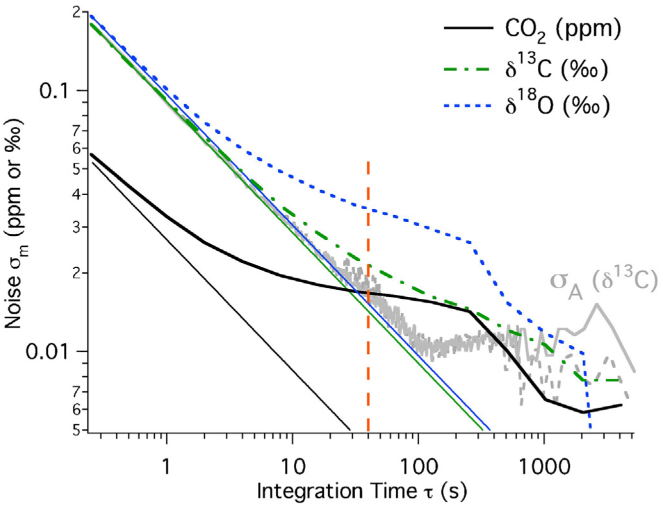

Fig. 3. QCLS noise (σ_m) in C (black, ppm), δ^{13}C (green, ‰), and δ^{18}O (blue, ‰) versus integration time (τ), for a calibration interval of 40 min and for nearly equal sample and reference cell CO$_2$ molar mixing ratios. The thin diagonal lines are the corresponding expectations for white noise. The vertical orange dashed line marks the dominant timescale of eddy transport at the Harvard Forest. For comparison, the Allan deviation for δ^{13}C is also plotted, without calibration (solid gray line) and with calibration (dashed gray line). (For interpretation of the references to color in this figure legend, the reader is referred to the web version of this article.)

i) The duration τ over which each measurement is averaged. Averaging reduces noise.

ii) The time span Δt in which the repetitions occur. Because of noise at long timescales (i.e. drifts), repeated measurements will typically be more precise (i.e. less noisy) if spread over 5 min than if spread over 3 h.

iii) The time interval Δt_{cal} between calibrations (if the data are calibrated). More frequent calibrations reduce the impact of instrument drift on noise. This is true even for $\Delta t < \Delta t_{cal}$; for example, a linearly drifting instrument response will increase σ_m for all Δt without calibration, but for no Δt with calibration.

iv) The duration τ_{cal} over which each calibration gas measurement is integrated (if the data are calibrated). A more precise calibration gas measurement (larger τ_{cal}) leads to better precision (and accuracy) in the calibrated sample measurement.

v) In the case of the present spectrometer, σ_m also depends on the difference ΔC between the sample and reference gas mixing ratios of CO$_2$ to dry air, as long as $\tau < 100$ s (owing mainly to laser frequency instability). Optimal precision for $\tau < 100$ s is achieved when $\Delta C = 0$. For $\tau > 100$ s, however, other sources of noise become dominant and σ_m becomes insensitive to ΔC (see Table 1).

In Fig. 3, we plot σ_m for C, δ^{13}C, and δ^{18}O versus the integration time τ. The values of the other parameters discussed above were: $\Delta C \approx 0$, $\Delta t = 160$ min, $\Delta t_{cal} = 40$ min, and $\tau_{cal} = 90$ s. These data are based on 3 h of continuous measurement from a compressed gas cylinder with $C \approx 450$ ppm. We estimated σ_m by performing simulated calibrations within this continuous time series, by treating some of the data as sample and some as calibration. The steps involved in this simulated calibration were: (1) subtract the mean to convert the time series into noise about the mean, (2) compute averages of duration τ_{cal} at intervals of Δt_{cal}, representing the measurement errors determined at each calibration, (3) linearly interpolate those errors between calibrations (discarding data beyond the last calibration to avoid extrapolation), and (4) subtract the resulting error time series from the noise time series to calibrate the data. We then divided the calibrated time series into bins of duration τ and computed σ_m as the standard deviation of the bin averages. The noise in Fig. 3 represents the instrument as it is used in the field.

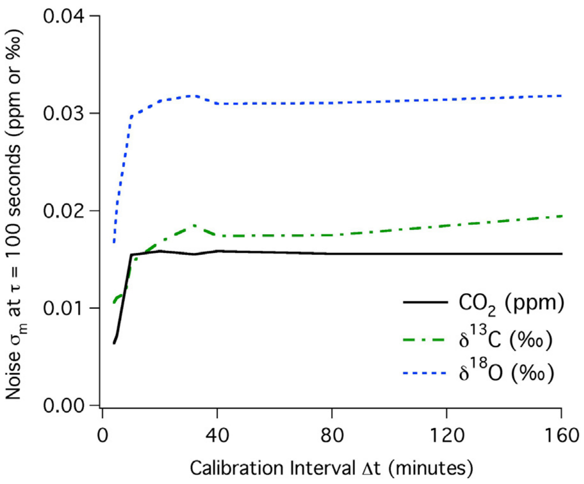

Fig. 4. QCLS noise (σ_m) in C (black, ppm), δ^{13}C (green, ‰), and δ^{18}O (blue, ‰) versus calibration interval (Δt_{cal}), for an integration time of 100 s and for nearly equal sample and reference cell CO$_2$ molar mixing ratios. (For interpretation of the references to color in this figure legend, the reader is referred to the web version of this article.)

Eddy covariance requires a high sample rate but integrates the data over the dominant timescale of eddy transport, roughly speaking. Our cospectra (see Section 4.3) show that eddy transport is significant at timescales from 1 to 1000 s at the Harvard Forest, with a peak around 50 s or 30 s (depending on whether you consider Fourier or multiresolution cospectra). Fig. 3 thus indicates that our effective instrument noise for EC is roughly 18 ppb for C, 0.02‰ for δ^{13}C, and 0.04‰ for δ^{18}O (marked by the orange vertical dashed line at 40 s).

Note that σ_m differs from the Allan deviation (Werle et al., 1993), which has also been used to characterize QCLS performance (e.g. Nelson et al., 2008). Whereas σ_m is the standard deviation of a sequence of averages, the Allan deviation σ_A is the standard deviation of a sequence of differences between adjacent averages. Because only adjacent averages are compared in computing σ_A, the time span Δt is effectively the same as the averaging time τ (and only this one timescale is involved in the computation). The value of σ_A for a given τ is therefore independent of noise at timescales longer than τ. In other words, for a given τ, σ_A quantifies only part of the noise: the part with a timescale shorter than τ. That property is useful for distinguishing contributions to the instrument noise at different timescales, but not for quantifying the overall instrument noise experienced in practice for a given averaging time and calibration interval. For comparison, we have plotted σ_A for δ^{13}C in gray in Fig. 3, with and without calibration. One can see that the Allan deviation reaches a minimum at an integration time of 100 s before increasing again, while σ_m decreases monotonically with increased integration time *ad infinitum*. Indeed, the standard deviation of repeated measurements can never increase with integration time, given a fixed time span Δt, even in the absence of calibration. At $\tau = 100$ s, σ_A is about half σ_m; this difference is due to the contribution to the latter of noise at timescales longer than τ.

The exceptional stability of the spectrometer is demonstrated in Fig. 4, where we plot σ_m versus Δt_{cal} for $\tau = 100$ s. The noise is nearly independent of Δt_{cal} for Δt_{cal} between 10 and 160 min (this is true regardless of τ), and reducing Δt_{cal} to 4 min (an impractically short calibration interval) reduces the noise by less than a factor of 2. Our 40-min calibration interval is thus a conservative choice – though we should mention that the instrument suffered occasional temperature regulation instabilities in 2011, which were

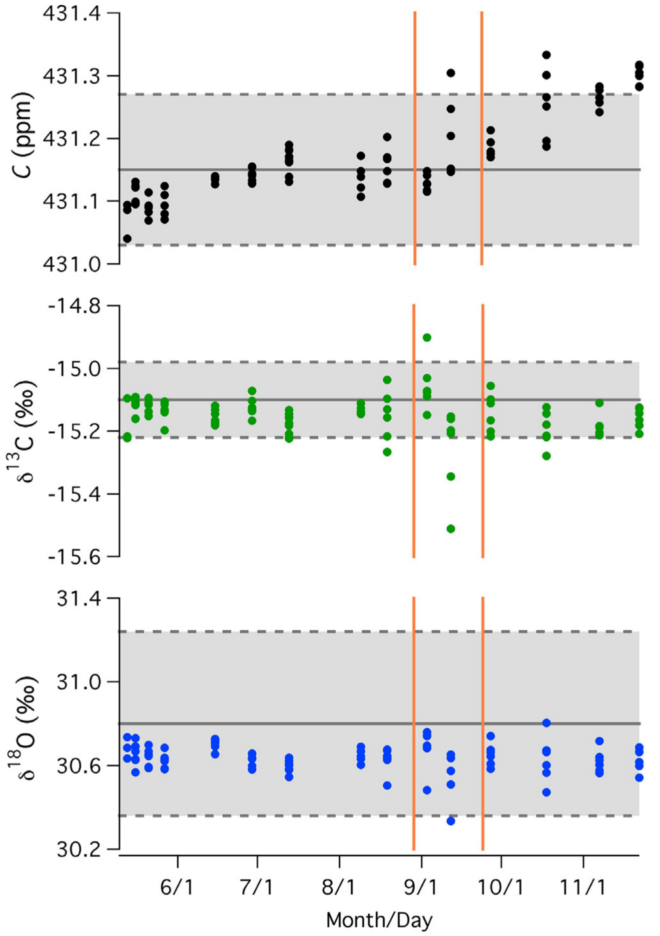

Fig. 5. Repeated QCLS measurements (dots) of C, $\delta^{13}C$, and $\delta^{18}O$ in a known target cylinder by linear interpolation between our 332 ppm and 496 ppm primary standard cylinders. The IRGA/IRMS values for the target cylinder are indicated by the horizontal solid lines, and the corresponding 95% confidence intervals are indicated by the gray regions. The vertical orange lines mark the period in September when an inferior instrument thermal regulation scheme was tested. (For interpretation of the references to color in this figure legend, the reader is referred to the web version of this article.)

rendered harmless by the 40-min Δt_{cal} but would have degraded performance with a longer Δt_{cal}.

4.2. Long-term calibration errors

Roughly every 2 weeks, whenever a pair of working tanks was installed or removed, they were calibrated against 3 primary standard cylinders, as described in Section 3.5. We took advantage of the primary standard measurements to test for long-term stability, by treating the 496 ppm and 332 ppm primary standards as high and low span working tanks, and measuring the 431 ppm primary standard as if it were unknown. Fig. 5 shows 101 such measurements between May and November. The solid gray lines indicate the pre-deployment characterization of the 431 ppm cylinder by IRMS (for the isotope ratios) or by IRGA (for the CO_2 molar mixing ratio). The gray shaded regions between the dashed lines indicate the 95% confidence intervals on the IRMS or IRGA measurements, which encompass the mean QCLS value in all three cases. The vertical orange lines indicate the period in September when an alternate (and inferior) instrument cooling arrangement was tested. Excluding that period, the QCLS standard deviations over the 6 months are 69 ppb (C), 0.05‰ ($\delta^{13}C$), and 0.06‰ ($\delta^{18}O$). The long-term isotope ratio noise of the QCLS is therefore less than the reported uncertainties of the IRMS characterization (0.06‰ for $\delta^{13}C$ and 0.22‰ for $\delta^{18}O$, based on 5 flask samples drawn from the cylinder and shipped from Massachusetts to Utah).

The noise in C is slightly greater than the reported uncertainty of the IRGA characterization (60 ppb), but only because of a very slow but clear drift. The cause of this drift remains unknown; it might result from a drift in one or more of the (steel) primary cylinders, or else from a drift in the instrument response. Re-characterization of our primary standards (which is planned) will not likely resolve the issue, given the measurement uncertainties, but we are examining possible instrumental causes. In any case, the magnitude of the drift is too small to significantly affect our results over the duration of this study.

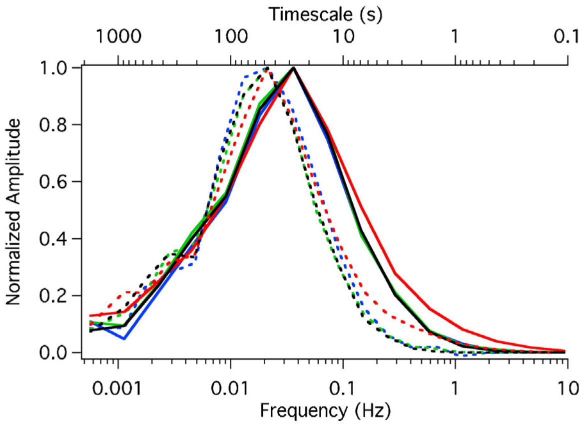

Fig. 6. Average frequency-weighted Fourier cospectra (dotted lines) and average multiresolution cospectra (solid lines) for sensible heat flux (red), CO_2 eddy flux (black), ^{13}C eddy isoflux (green) and ^{18}O eddy isoflux (blue), for the period July 16th–21st. These cospectra have been normalized to their peak amplitudes for comparison. Prior to averaging, each individual cospectrum was made positive by multiplication by the sign of the sum of the points between 0 and 60 s. The three multiresolution CO_2 cospectra lie on top of one another, apart from noise. (For interpretation of the references to color in this figure legend, the reader is referred to the web version of this article.)

4.3. Cospectra

Fig. 6 compares average multiresolution cospectra (MRCs) and frequency-weighted Fourier cospectra for the sensible heat flux, the CO_2 flux, and the two isofluxes. These averages were computed over the period July 16th–21st. Prior to averaging, each individual cospectrum was made positive by multiplication by the sign of the sum of its points between 0 and 60 s but was not otherwise normalized. Longer timescales were excluded from the sign determination to avoid contamination by low-frequency noise. By not normalizing the individual cospectra before averaging, we avoid amplifying the cospectral noise in periods with small fluxes. The trade off is that the w-C and w-T cospectra in Fig. 6 are weighted to slightly different periods: the w-T cospectra to periods with large heat flux, and the w-C cospectra to periods with large CO_2 flux. Nonetheless, those periods largely coincide.

The first point of interest in Fig. 6 is that the Fourier cospectra have nearly the same shape as the MRCs, but the former peak at about 50 s while the latter peak at about 30 s. This result is consistent with the argument in Howell and Mahrt (1997) that the Fourier cospectra are biased to longer timescales by the quasi-periodic nature of turbulent transport. Thus the MRC peak may be the more representative of the scale of the turbulent eddies at the Harvard Forest. However, Fourier and multiresolution cospectra also depict the spectral distribution of the covariance differently: a nonzero value at 1 s in an MRC does not mean that an oscillation with a period of 1 s is present in the time series; it means instead that an integration period of 1 s yields a different covariance than does an integration period of 0.5 s, as would be the case even if the only signal present were a perfect oscillation at 2 Hz. Thus an MRC is expected to be weighted to higher frequencies than the corresponding Fourier cospectrum. Hereafter, we use MRCs only because they are easier to generate and work with.

The second point of interest in Fig. 6 is that the CO_2 flux and isoflux cospectra of a given type (Fourier or MRD) are indistinguishable from one another but fall below the corresponding heat flux cospectrum at high frequency. This behavior is expected given the finite time response of the CO_2 sampling system (dependent on volume, flow rate, and sample rate) and the ~0.5 m separation of the CO_2 inlet from the sonic anemometer. We correct for the high-frequency attenuation caused by the CO_2 sampling system by comparing the *w-C* MRCs to the *w-T* MRCs and making the well-established assumption of cospectral similarity (i.e. all cospectra have the same shape). The specifics of our method require a few paragraphs of explanation.

What we seek is a correction curve describing the factor by which we should multiply each point in a CO_2 flux or isoflux MRC to recover the MRC we would have observed without attenuation. Assuming cospectral similarity – and negligible attenuation of the temperature and wind data – this correction curve is given simply by the ratio of the *w-T* MRC to the *w-C* MRC, provided each MRC is first normalized to its value at some timescale outside the attenuated range. We choose to normalize to the mean value of the MRC between 10 and 100 s, which is the region where the turbulence peak is usually found, and where we observe neither high-frequency attenuation nor low-frequency noise (discussed below). For convenience, we will call the 10–100 s mean the *peak mean*. Given that the measured isoflux MRCs have the same shape as the measured *w-C* MRC, the *w-C* correction curve applies to them as well.

The effect of signal attenuation on a cospectrum, in general, depends on the shape of the cospectrum. Thus the correction curve defined above depends not only on the (unchanging) CO_2 sampling system, but also on (changing) atmospheric conditions – chiefly the mean wind speed and the atmospheric stability. Unfortunately, calculating the correction curve for each individual EC integration period is problematic due to noise in the MRCs, especially in periods with small fluxes (e.g. dawn and dusk). We therefore constructed a lookup table of correction curves by averaging all our *w-T* and *w-C* MRCs (~3000 of each) in nested quantiles of the mean wind speed $\bar{u}$ and the nondimensional stability parameter z/L, where z is the canopy height and L is the Monin–Obukhov length (Foken, 2006). (Although Monin–Obukhov similarity theory is invalid below 2 or 3 times the canopy height (Foken, 2006), z/L as determined at our flux measurement height of 29 m can give at least a rough indication of atmospheric stability: negative values of z/L indicate instability, near-zero values indicate neutrality, and positive values indicate stability.) The correction curve for a given combination of $\bar{u}$ and z/L was computed as the ratio of the average *w-T* MRC to the average *w-C* MRC in the appropriate quantile. For z/L, we used 5 quantiles, and within each of those, we nested 12 quantiles of $\bar{u}$ (thus there were 60 bins in total). The number of quantiles was chosen based on trial and error and inspection of the resulting correction curves, balancing the desires to reduce noise and to resolve the pattern of variation of the correction curve. For the final lookup table, the correction factor at each MRC timescale was smoothed versus wind speed (using a Loess filter) in order to reduce noise with minimal smearing of the patterns of variation. Periods for which the absolute magnitude of the uncorrected heat flux was less than 10 W/m^2, or u^* was less than 0.17, were excluded from the bin averaging. The correction curves were set to 1 at timescales larger than 30 s to avoid spurious corrections due to low-frequency noise.

As noted earlier, precise comparison of average MRCs like those in Fig. 6 is problematic because they are weighted to slightly different EC integration periods. We therefore devised the following method for averaging MRCs within each bin. First, we normalized each individual MRC to its peak mean as defined above. We then weighted each normalized MRC, whether it be *w-T* or *w-C*, by the product of the *w-T* MRC peak mean and the *w-C* MRC peak mean for the same EC integration period. In this way, the average *w-C* and *w-T* MRCs were weighted to exactly the same periods, which were those periods with large (positive or negative) fluxes of both heat and CO_2.

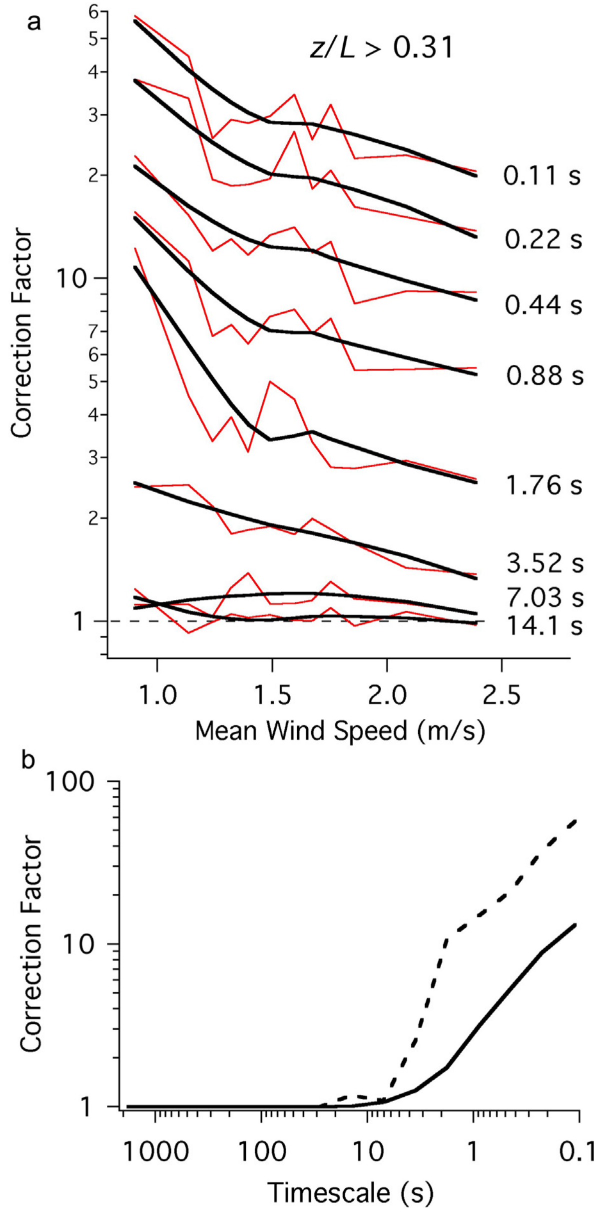

Fig. 7. (a) Log plots of the CO_2 MRC correction factor versus wind speed, at 8 different MRC timescales, for $z/L > 0.31$. The red lines show the computed attenuations in 12 wind speed bins. The black lines are smoothed versions obtained with a Loess filter. The MRC correction factor is used to scale the CO_2 flux and isoflux MRCs in order to correct for high frequency signal attenuation. (b) The largest and smallest MRC correction curves in the lookup table. The solid line is for $z/L < -0.24$ and a mean wind speed of 2.2 m/s. The dashed line is for $z/L > 0.31$ and a mean wind speed of 0.9 m/s (i.e. the leftmost points in (a)). (For interpretation of the references to color in this figure legend, the reader is referred to the web version of this article.)

The variation of the correction curve with z/L and $\bar{u}$ is clear and systematic, with the smallest corrections occurring in unstable conditions and at moderate wind speeds (~2 m/s). Fig. 7a shows the original and the smoothed correction factor versus $\bar{u}$, for $z/L > 0.31$,

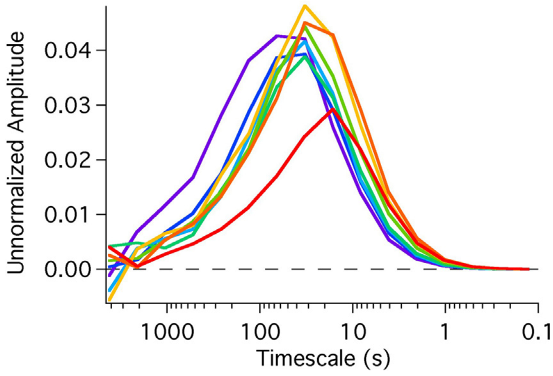

Fig. 8. 70-min multiresolution cospectra for CO_2, averaged by mean wind speed, for the entire 2011 growing season (but excluding times when $u^* < 0.17$ m/s). Color is on a rainbow scale from violet (lowest mean wind speed bin, centered on 0.66 m/s) to red (highest mean wind speed bin, centered on 5.0 m/s). Prior to averaging, each individual cospectrum was multiplied by the sign of the sum of the cospectral points between 0 and 60 s, but not otherwise normalized. (For interpretation of the references to color in this figure legend, the reader is referred to the web version of this article.)

while Fig. 7b shows the largest and smallest correction curves in the lookup table. We tried additional binning by wind direction, but the added noise associated with the reduced number of cospectra in each bin masked any directional variation. On average, our correction for high-frequency attenuation increases the absolute magnitude of the eddy flux by 0.48 μmol m^{-2} s^{-1}.

Having explained our correction for high-frequency attenuation, we return to Fig. 6. The third and final point of interest in Fig. 6 is that the cospectra do not quite reach zero at low frequency, raising the possibility that 30 min might be too short an EC integration period to capture all the eddy flux at the Harvard Forest under some conditions. To test this possibility, we combined our 30 min (1800 s) EC integration periods in pairs to form 70 min (4200 s) periods, each with a 10 min gap in the middle for calibration and canopy profile measurements. As required by MRD, a regular grid of 2^{16} points was made to span the 70 min, and those points interpolated across the gap had their values of w' set to zero so that they would not contribute to the MRC, which was scaled by ~6/7 to account for the reduced number of points used. The nature of MRD (recalculating the mean covariance as the time series is successively halved) is such that introducing a gap in the way just described has no effect on the MRC (barring any difference in the properties of the turbulence inside and outside the gap).

Fig. 8 shows our 70-min CO_2 MRCs bin-averaged by $\bar{u}$. As in Fig. 6, each individual cospectrum was made positive by multiplication by the sign of the sum of its points between 0 and 60 s. Fig. 8 shows that the MRC is effectively zero at 70 min even for the lowest $\bar{u}$, i.e. there is no significant flux signal past 35 min. The same is true when we restrict the averaging to unstable atmospheric conditions ($z/L < 0$) (results not shown). As a final check, we compared our 70-min CO_2 eddy fluxes with a linear interpolation of our usual 30-min fluxes onto the 70-min time grid, throughout the growing season (results not shown). We found that the two values typically agreed to within 0.5 μmol m^{-2} s^{-1}, with the mean difference over the season being just 0.02 μmol m^{-2} s^{-1} and the root-mean-square difference over the season being 2.4 μmol m^{-2} s^{-1}. When there was disagreement, the 30-min fluxes were typically less noisy and more plausible (the 70-min fluxes being more prone to being near zero or negative at night, due to noise). Thus 70 min is probably too long an integration period at the Harvard Forest, capturing more low-frequency noise but no more signal than is captured in 30 min.

4.4. *(Iso)fluxes*

Our isotopic flux data can be used to compute the individual isotopologue fluxes and the ^{13}C and ^{18}O isofluxes (see Section 2). The data can also be used, of course, to compute the total CO_2 flux. All our isotopic flux data are available in the Harvard Forest Data Archive (online at http://harvardforest.fas.harvard.edu/data-archive) and on the Saleska group website (http://www.eebweb.arizona.edu/faculty/saleska/lab.htm). We encourage researchers to use these data to constrain or test isotope-enabled ecosystem–atmosphere models. Here we illustrate a couple of broad patterns.

In Fig. 9, we attempt to provide a sense of the diel and seasonal variations in NEE, I_N^{13}, and I_N^{18} by plotting them over two 5-day periods, one at the beginning and one at the end of summer. Both daytime photosynthetic and nighttime respiratory activity are clearly reduced by the end of summer. Throughout, I_N^{13} is nearly proportional to NEE, and always of opposite sign, as expected for variations of only a few ‰ in δ_N^{13}. On the other hand, I_N^{18} tends to be roughly proportional to NEE at night and in the mornings only, indicating a strong change in δ_N^{18} over the course of the day.

We explore that diurnal change in Fig. 10, where we show monthly average diel cycles of δ_N^{18}, smoothed to 2 h. To reduce the influence of periods with low flux and thus highly uncertain δ_N^{18}, we have flux-weighted the average δ_N^{18} for each diel time bin by calculating it as the slope of a straight line fit to I_N^{18} versus F_N in that bin. The behavior of δ_N^{18} is fairly consistent from month to month, with a decrease from roughly 30 to 10‰ over the course of the daylight hours, and then a sudden return to the nighttime value around sunset. The same pattern appeared in Fig. 9b of Sturm et al. (2012) (also a forest study), and a similar pattern but with a different nighttime value appeared in Fig. 15d of Griffis et al. (2008)

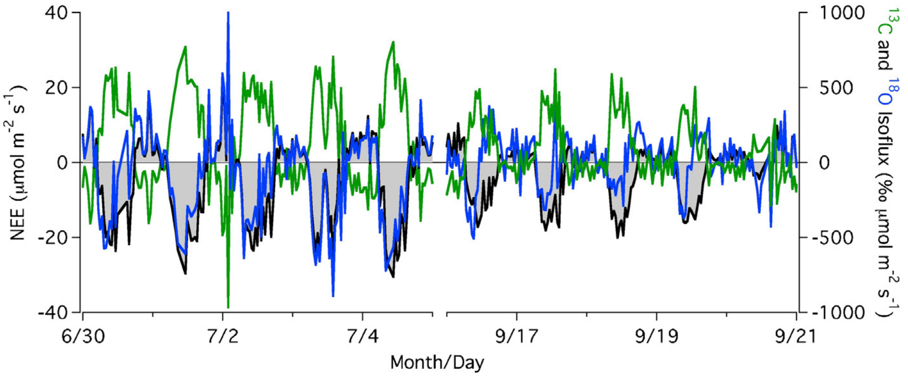

Fig. 9. NEE (black), the ^{13}C isoflux (green), and the ^{18}O isoflux (blue) for two periods, one at the beginning and one at the end of summer, 2011. (For interpretation of the references to color in this figure legend, the reader is referred to the web version of this article.)

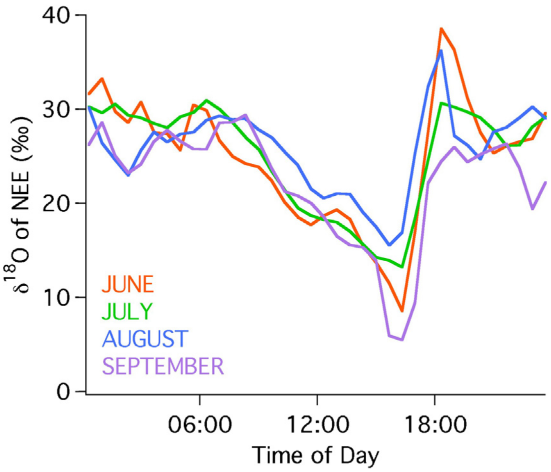

Fig. 10. Monthly average diel cycles of δ_N^{18} for June (orange), July (green), August (blue), and September (purple). Cycles have been smoothed to 2 h. Details of the averaging procedure are given in the text. (For interpretation of the references to color in this figure legend, the reader is referred to the web version of this article.)

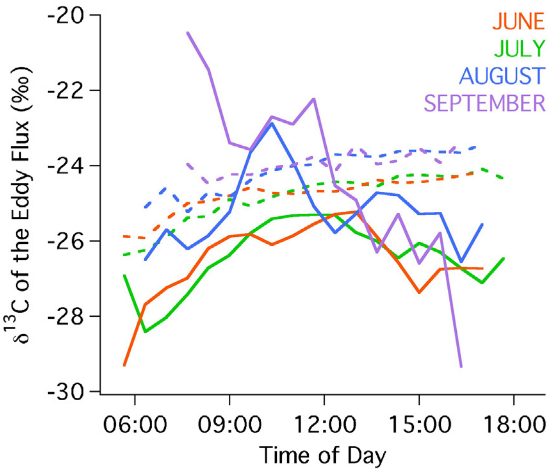

Fig. 11. Monthly average diel cycles of δ_E^{13}, as measured by EC (solid lines) and as estimated by the EC/flask approach (dashed lines), for June (orange), July (green), August (blue), and September (purple). The EC cycles have been smoothed to 2 h, and only times for which the average CO_2 flux was less than $-2\ \mu\text{mol m}^{-2}\ \text{s}^{-1}$ are shown. Details of the averaging procedure are given in the text. (For interpretation of the references to color in this figure legend, the reader is referred to the web version of this article.)

(an agricultural field study). Note that those studies used the VPDB scale for δ^{18}O rather than the VSMOW scale used here. We suggest that the decrease in δ_N^{18} over the course of the day should result from a gradual increase in the δ^{18}O of leaf water by evaporative enrichment, because: (1) CO_2 readily exchanges ^{18}O with leaf water due to the action of carbonic anhydrase, so that the δ^{18}O of leaf CO_2 would also increase over the course of the day, (2) both $^{18}O^{12}C^{16}O$ and $^{12}C^{16}O_2$ are less abundant in the leaf than in the atmosphere due to photosynthetic drawdown, so that an increase in the δ^{18}O of leaf CO_2 means a decrease in the atmosphere-leaf gradient of $^{18}O^{12}C^{16}O$ relative to that of $^{12}C^{16}O_2$, and (3) a decrease in the atmosphere-leaf gradient of $^{18}O^{12}C^{16}O$ relative to that of $^{12}C^{16}O_2$ would effect a reduction in the flux of $^{18}O^{12}C^{16}O$ relative to that of $^{12}C^{16}O_2$, which is to say a reduction of δ_N^{18}. The sudden return of δ_N^{18} to 30‰ around sunset may indicate that during the day, when photosynthesis dominates NEE, δ_N^{18} is primarily influenced by leaf water, while at night, when root and soil respiration dominate NEE, the primary influence is soil water, which does not become enriched in ^{18}O as rapidly as leaf water.

4.5. EC/flask comparison

Fig. 11 compares monthly average diel cycles of δ_E^{13} obtained by direct EC measurement and by the EC/flask method. The corresponding cycles in δ_N^{13} are nearly indistinguishable from those in δ_E^{13}, but we show δ_E^{13} for more direct comparison of the two methods. To focus on the photosynthetic period, we have only shown data for the portion of the day when the monthly average eddy flux was less than $-2\ \mu\text{mol m}^{-2}\ \text{s}^{-1}$. To further reduce the influence of periods with low flux and thus highly uncertain δ_E^{13}, we have flux-weighted the average δ_E^{13} for each diel time bin by calculating it as the slope of a straight line fit to I_E^{13} versus F_E in that bin. The dashed lines indicate the EC/flask values (following the implementation of Knohl and Buchmann, 2005) while the solid lines indicate the pure EC values, which have been smoothed to 2 h. Even around midday (when flasks would be filled), the EC/flask values in June, July, and August are biased high relative to the EC values by about 1‰. Moreover, the direct EC measurements reveal diurnal patterns in δ_E^{13} that the EC/flask method, having assumed a constant relationship between δ^{13}C and C, cannot detect. These patterns likely reflect a shifting balance between diffusive and biochemical limitations on photosynthesis over the course of the day, which is important for isotopic flux partitioning. The direct EC measurements also indicate an evolution of these patterns over the growing season, with a trend toward more diffusive limitation (less light limitation) in the mornings, while seasonal variation using the EC/flask method is limited to a wholesale shift of the diurnal curve.

Another problem with the EC/flask method is that the results are sensitive to the assumptions and data selection criteria used, but there is no best choice for those assumptions and criteria. For example, we can compare the well-reasoned EC/flask implementation discussed thus far (omitting samples below 2 m, using a δ^{13}C versus C fit, restricting sampling to midday) with a crude implementation that uses samples from all tower inlet heights, at all times of the day and night, in a single month-long global Keeling fit. This crude implementation, in other words, treats δ_E^{13} as a constant over the entire month. Nonetheless, it typically does as well as the well-reasoned implementation, with a bias of similar magnitude in the opposite direction (roughly −1‰ at noon rather than +1‰).

An EC/flask bias of 1–2‰ in daytime δ_N^{13} would be expected to lead to nearly the same bias in the isotopic signature of photosynthesis estimated in the course of isotopic flux partitioning, because daytime NEE is dominated by photosynthesis. In this light, the ∼+2‰ offset between the isotopic signatures of photosynthesis and respiration observed and discussed in Knohl and Buchmann (2005) was probably within the uncertainty of the EC/flask method. For more on errors in partitioning, see Section 4.8.

4.6. Limits on noise in the isotopic flux

Though we restrict our discussion in this section to $^{13}CO_2$ and $^{12}CO_2$, the same arguments apply to $^{18}O^{12}C^{16}O$, for which the instrument noise is similar.

In order to investigate the contribution of instrument noise to the total noise in the eddy flux F_E, the eddy isoflux I_E^{13}, and the isotopic composition of the eddy flux δ_E^{13}, we analyzed simulated data for the period from July 16th to 21st. The advantage of simulated data is that the signal and the noise are known, so that we can quantify exactly how the noise propagates into derived quantities like δ_E^{13}. The first task in the simulation was to generate ‘true’ signals for w, C, and δ^{13}; we denote these simulated signals by a subscript T. For w_T, we used our real measured w', whose measurement noise was <0.001 m/s and therefore negligible. For C_T and δ_T^{13}, we tried two approaches, which we will call the *perfect-correlation* and *zero-correlation* approaches.

In the perfect-correlation approach, we assumed the true variation of C at the EC inlet to be perfectly correlated with w'. (In reality, there is only a partial correlation, as the w-C cospectrum is weighted to substantially lower frequencies than the w power spectrum.) Thus we generated $C_T = aw' + 380$, where the constant a was chosen separately for each 30-min EC integration period in order to make the covariance $\overline{w'_T C'_T}$ equal to our measured covariance $\overline{w'C'}$ and thereby ensure a realistic magnitude for the variation in C_T. For δ_T^{13}, we assumed a Keeling line with a source signature of -26‰, a background signature of −9‰, and a background mixing ratio of 380 ppm, and then calculated δ_T^{13} from C_T. Though Keeling lines are not valid when there is both a source and a sink of CO_2, they can serve as a sufficient approximation for our purposes here. An approximate value suffices also for the constant a.

In the zero-correlation approach, we simply set $C_T = 380$ ppm and $\delta_T^{13} = -90$ ‰, with no variations, so that the true fluxes and isofluxes would be zero.

Having generated C_T and δ_T^{13} by one or the other approach, we then added randomly generated noise to each signal at several timescales such that the overall noise power spectrum was nearly indistinguishable from our corresponding real instrument noise power spectrum. (For a description of our real instrument noise, see Section 4.1.) We then used the resulting "instrument noise only" time series to compute F_E, I_E^{13}, and δ_E^{13} as usual – though in order to compute δ_E^{13} in the zero-correlation approach, we had to treat our measured eddy (iso)fluxes as approximate true values and add them to the computed zero-centered (iso)fluxes, before dividing the isoflux by the flux (otherwise we would be dividing ∼0 by ∼0). For both approaches, we repeated the noise generation and EC calculation steps 64 times for each EC integration period in order to determine standard deviations.

The perfect-correlation and zero-correlation approaches gave nearly indistinguishable results, indicating that the detailed structure of the true C and δ^{13} signals is unimportant for the purposes of simulating the propagation of noise from those quantities. The detailed structure of the w signal is important, however; indeed the task of the simulations is to quantify how instrument noise produces spurious correlations with w'.

We found that instrument noise in C contributes a mean standard deviation of 0.024 μmol m^{-2} s^{-1} to F_E, with the noise for individual integration periods ranging from 0.0077 to 0.062 μmol m^{-2} s^{-1} depending on the magnitude of the fluctuations in C (which get larger as F_E gets larger and as the fluctuations in w get smaller). Instrument noise in C and δ^{13} contributes a mean standard deviation of 18‰ μmol m^{-2} s^{-1} to I_E^{13}, with individual periods ranging from 7.7 to 35‰ μmol m^{-2} s^{-1}, and a mean standard deviation of 5.4‰ to δ_E^{13}, with individual periods ranging from 0.53 to 64‰. Note that the mean standard deviation for δ_E^{13} is dominated by large values in periods with low flux (i.e. those periods we care least about) because δ_E^{13} becomes undefined as F_E approaches zero. The standard deviation for δ_E^{13} is typically about 1.5‰ around midday.

Having quantified our instrument noise, it remains to estimate the total noise, which can be nuanced because the true net CO_2 exchange can fluctuate significantly due to changing cloud cover. Nonetheless, by considering select periods (especially night), we can conclude that the standard deviation of the total point-to-point noise in F_E is roughly 1 μmol m^{-2} s^{-1} while that in I_E^{13} is roughly 25‰ μmol m^{-2} s^{-1}. Thus the instrument noise contribution to F_E is negligible while that to I_E^{13} is significant, in agreement with the prediction in Saleska et al. (2006) for an instrument with the nearly the present specifications at this site.

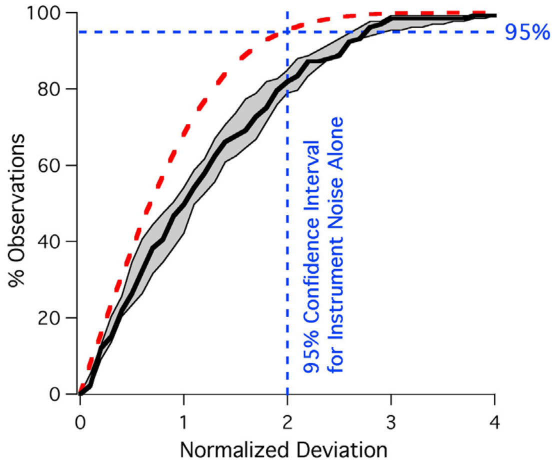

Fig. 12. The observed cumulative distribution of δ_E^{13} about its smoothed variant (thick black line), and the expected cumulative distribution of δ_E^{13} resulting from instrument noise alone (red dashed line). The deviations have been normalized to the standard deviation expected for instrument noise alone, on a period-by-period basis. The thin black lines bounding the gray region are observed distributions obtained using extremely mild and extremely strong smoothing. The 95% confidence interval and 95% observations line are marked in blue. (For interpretation of the references to color in this figure legend, the reader is referred to the web version of this article.)

We have quantified the relative importance of instrument noise to δ_E^{13} more precisely by assuming that its true value, averaged over the ecosystem, varied over the diel cycle but did not fluctuate measurably from hour to hour. This assumption was supported a posteriori by the fact that our estimates of the ratio of total noise to instrument noise were actually slightly larger, on average, when using only nighttime data. We began by smoothing the measured values of δ_E^{13} using Igor's built-in Loess (i.e. local regression) filter with rejection of extreme values. The degree of smoothing by a Loess filter is characterized by the smoothing parameter α, which describes the proportion of the dataset used for the local regression around each point. Given our 6-day dataset, the value $\alpha = 0.15$ effectively removed fluctuations with periods less than about 6 h. We then took the variations of our measured δ_E^{13} about the smoothed δ_E^{13} to approximate the total noise in δ_E^{13}. Because the degree of smoothing was somewhat arbitrary, we tested two extremes as well, corresponding to $\alpha = 0.09$ (no fluctuations faster than ∼3 h) and $\alpha = 0.5$ (no fluctuations faster than ∼2 days).

Our results are presented in Fig. 12, where we compare the observed cumulative distribution of δ_E^{13} about the smoothed, "true" curve to the cumulative distribution expected for instrument noise alone, according to our noise simulation. To allow this comparison across integration periods, members of each distribution were first normalized to the standard deviation expected from instrument noise alone for their particular period. Thus the curve shown for instrument noise alone is simply the cumulative Gaussian distribution. One can see, first, that the observed distribution is also roughly Gaussian, and second, that the effect of α on the cumulative distribution is minor; $\alpha = 0.15$ gives the ratio of total noise to instrument noise as ∼1.5, while $\alpha = 0.09$ gives the ratio as ∼1.3 and $\alpha = 0.5$ gives it as ∼1.7. Throughout this plausible range, the contributions of instrument and non-instrument noise to the total noise are roughly equal, with the ratio of non-instrument to instrument noise being at least 0.8 and at most 1.4 ($1.3^2 = 1^2 + 0.8^2$ and $1.7^2 = 1^2 + 1.4^2$). Given that significant diel variation in δ_E^{13} is expected, a reasonable value is 1.1, obtained using $\alpha = 0.15$. Thus we can say that improvements to the instrument precision will yield only minor improvements to the overall precision with which δ_E^{13} can be measured by eddy covariance. Even progressing to a perfect instrument, the noise in δ_E^{13} should only be reduced by about 25%.

In principle, non-instrument noise in F_E, I_E^{13}, and δ_E^{13} can arise either because of a randomly varying disparity between the CO_2 isotopologue mixing ratios (to dry air) in the spectrometer and those at the sonic anemometer (after accounting for the sampling system transit time), or else because of a randomly varying disparity between the CO_2 isotopologue fluxes at the sonic anemometer and those averaged over the ecosystem. In practice, only the latter cause is plausible – and it is not merely plausible, but probable. Ecosystem–atmosphere gas exchange is a three-dimensional, volumetric process that we attempt to measure at a single point in space; as a result, and as noted in Section 2, the EC method is valid only under the assumption of horizontal homogeneity. Because the ecosystem, the landscape, and the air motions at the Harvard Forest are all significantly heterogeneous on both small and large scales, some fluctuation of the measured eddy flux (and its isotopic composition) about the ecosystem average is expected.

4.7. *Sensitivity of the isotopic flux to EC data processing*

Our conclusion in Section 4.6 that the uncertainty in δ_E^{13} is limited jointly by instrument noise and by horizontal heterogeneity is similar to the conclusion recently reported by Sturm et al. (2012), that their uncertainty in δ_E^{13} was limited jointly by instrument noise and by "random error associated with EC data processing". There are, however, two problems with this latter conclusion. The first borders on semantic but is nonetheless important: the random error in question cannot derive from the processing of the data; it must derive from the data themselves (e.g. because they are single-point measurements of a volumetric exchange process, as discussed in Section 4.6). The processing is deterministic. Only the data possess a random element. The second problem is that the analysis presented in Sturm et al. (2012) was not capable of assessing the contribution of instrument noise to the uncertainty in δ_E^{13}. Sturm et al. (2012) considered all the EC measurements of δ_E^{13} in their one-month study as an ensemble and examined the statistical effects on that ensemble of various changes to the EC calculation – such as using triple rather than double rotation of the wind coordinates, or using linear detrending rather than simple Reynolds block averaging. They found that the differences in δ_E^{13} between one version of the calculation and another were randomly scattered about zero. That is, a change to the calculation made some measurements of δ_E^{13} go up and others go down, with no significant shift in the mean. They also found that the magnitude of the scatter in the differences, for each of the calculation changes they tested, was as large as the magnitude of the scatter induced by adding simulated instrument noise (of the same magnitude as their real instrument noise) to their data. They concluded that the uncertainty in δ_E^{13} for a given integration period resulted as much from "inherent EC uncertainty" as from instrument noise.

In drawing that conclusion, it was implicitly assumed that the scatter in the differences in δ_E^{13} between one version of the EC calculation and another resulted from some source of noise other than the instrument (i.e. "inherent EC uncertainty"). But any kind of noise in the data, including instrument noise, can produce those same scattered differences in δ_E^{13} between one version of the EC calculation and another. The magnitude of the scatter depends on the pattern of noise (but not its origin) and on how each version of the calculation translates that noise into δ_E^{13}. So, in principle, the results reported in Sturm et al. (2012) might have been obtained for any weighting of instrument and non-instrument noise.

We should also report that we performed four of the sensitivity analyses described in Sturm et al. (2012) on our own data, and found that the scatter in δ_E^{13} associated with each change to the EC calculation was much smaller than the scatter associated with the instrument noise described in Sturm et al. (2012). We chose one sensitivity analysis of each type represented in Sturm et al. (2012): instrument noise, averaging scheme, integration period, and wind coordinate rotation. Our results are presented in Fig. 13, whose box and whisker plots have been crafted for direct visual comparison with those in Sturm et al. (2012). As in Sturm et al. (2012), we used double rotation and block averaging over 30 min for our reference calculation. The instrument noise added was 4 Hz Gaussian white noise with a standard deviation of 0.13 ppm in C and 0.38‰ in $\delta^{13}C$; this noise exactly follows the description in Sturm et al. (2012), and is therefore about twice as large as our actual instrument noise, though we had to scale the standard deviations from 10 to 4 Hz values by dividing by $\sqrt{10/4}$. Unsurprisingly, the scatter resulting from this noise was nearly the same here (8.2‰) as in Sturm et al. (2012) (8.8‰). The scatter associated with the change to triple rotation, on the other hand, was 42 times smaller here (0.23‰ versus 9.7‰). The scatter for the switch to linear detrending was 4 times smaller here (1.2‰ versus 5.0‰), and the scatter for the switch to 15-min (block) averaging was 7 times smaller here (1.0‰ versus 7.0‰). So at our site, using our spectrometer, the particulars of the EC data processing had a negligible influence on δ_E^{13} even in a stochastic sense. Note that these results do not imply that the simulated instrument noise would be the dominant source of uncertainty in δ_E^{13} at our site; they might simply indicate that the various versions of the EC calculation do not differ much in how they translate the data noise into noise in δ_E^{13}. We excluded periods when $u^* < 0.17$ m/s (Urbanski et al., 2007) from these statistical tests, although this filtering did not much affect the results.

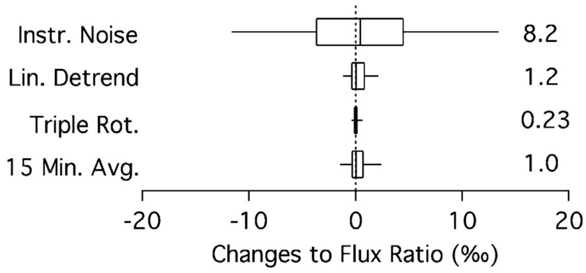

Fig. 13. Box and whisker plots directly comparable to those in Sturm et al. (2012), showing the distribution of changes to δ_E^{13} associated with increased instrument noise and three changes to the EC calculation. Boxes span the 25th to 75th percentiles and whiskers span the 10th to 90th percentiles. Numbers at right are the box widths.

4.8. *Prognosis for isotopic flux partitioning*

A proper treatment of the isotopic partitioning of NEE is too elaborate to include here, and is therefore to be presented in a separate article. Nonetheless, we can give a brief indication of the potential for partitioning using the present measurements.

Isotopic flux partitioning amounts to solving the combined mass balance equation for $^{12}CO_2$ and $^{13}CO_2$:

$$F_A = \frac{(\delta_N^{13} - \delta_{NR}^{13})}{(\delta_A^{13} - \delta_{NR}^{13})} F_N \tag{5}$$

where F_A is the net photosynthetic assimilation flux, and δ_A^{13} and δ_{NR}^{13} are the carbon isotope signatures of net photosynthetic assimilation and of nonfoliar ecosystem respiration, respectively (Saleska et al., 2006). The difference between these signatures, appearing as the denominator in Eq. (5), is called the isotopic disequilibrium. It is clear that partitioning is impossible when the signatures are identical, and that the error in F_A becomes infinite as the disequilibrium approaches zero (for a given δ_N^{13}). In line with expectations, we have found that the actual disequilibrium at the Harvard Forest is roughly 2‰. Thus it would seem impractical to partition NEE if the uncertainties in δ_A^{13}, δ_{NR}^{13}, and δ_N^{13} have standard deviations on the order of 1‰.

However, in isotopic flux partitioning as conceived by Bowling et al. (2001) and developed thereafter, δ_A^{13} is not measured; rather, it is related to F_A by additional equations describing CO_2 diffusion within the leaf, and solved for as an unknown alongside F_A. Error in δ_N^{13} or δ_{NR}^{13} is thus divided between δ_A^{13} and F_A, so that the latter is less sensitive to said error than expected.

Put another way, F_A is constrained by its relationship to δ_A^{13}. For example, if isotopic measurement error were to cause the magnitude of the retrieved F_A to increase from its true value, then the retrieved δ_A^{13} would have to move toward the diffusion-limited extreme of ∼−13‰, which the equations could not support given that: (1) both δ_N^{13} and δ_{NR}^{13} are fixed by measurement at around −25%, and (2) the photosynthetic flux is a greater contributor to F_N than is the respiratory flux (through most of the daylight hours). Going in the other direction, δ_A^{13} moves toward the biochemistry-limited extreme of ∼−36‰, which is equally insupportable except for a secondary, ecologically implausible solution to the equations near $F_A = 0$, where the value of δ_A^{13} becomes irrelevant.

In practice, we find that an intentionally introduced error of +1‰ in δ_N^{13} induces an error of about +0.5‰ in δ_A^{13} and an error varying between just −1 and −2 μmol m^{-2} s^{-1} in F_A (+1 and +2 μmol m^{-2} s^{-1} in F_{NR}). Thus the present measurement precision of 1.5‰ in δ_N^{13} around midday should be sufficient for partitioning individual 40-min measurements of NEE with an uncertainty of about 2 μmol m^{-2} s^{-1}.

5. Conclusion

We have presented eddy covariance measurements of the ecosystem–atmosphere exchange of $^{13}C^{16}O_2$, $^{18}O^{12}C^{16}O$, and $^{12}C^{16}O_2$ at the Harvard Forest over the 2011 growing season. This isotopic EC measurement dataset is the first to extend to the seasonal timescale, and only the third ever recorded in any ecosystem. We have featured three prominent patterns. First, the ^{13}C composition of NEE exhibits a pattern of daytime variation likely reflecting a shifting balance between the diffusive and biochemical limitations on photosynthesis. Second, the ^{18}O isoflux exhibits features associated with evaporative ^{18}O enrichment of leaf water over the course of the daylight hours. Third, there are clear seasonal variations in both isofluxes and in the ^{13}C composition of NEE. The ^{18}O composition of NEE is more consistent from month to month.

Using our measurements, we have demonstrated that the previously used EC/flask method for approximating the ^{13}C isotopic composition of NEE cannot resolve the daytime variation just mentioned, and can be biased relative to pure EC measurements, on a monthly timescale, by 2‰.

We have also rigorously assessed the limiting sources of uncertainty in our measurements, finding in particular that uncertainty in the isotopic composition of NEE is jointly limited by instrument noise and by ecological and environmental heterogeneity, so that further improvements to instrument performance will be of little benefit. We have also clarified that the EC data processing does not contribute significantly to the uncertainty, contrary to the implication in Sturm et al. (2012). Instrument noise was determined based on our detailed characterization of the new cryogen-free, continuous-wave, quantum cascade laser spectrometer that was used to measure the CO_2 isotopologue molar mixing ratios. The precision and stability of this spectrometer – when its electronics are housed in a thermally regulated container – are unprecedented among laser spectrometers, and on par with isotope ratio mass spectrometers.

Finally, we have argued that the precision with which we can measure the isotopic composition of NEE is sufficient to provide insight into the biological mechanisms controlling ecosystem-scale carbon balance, and in particular to partition NEE into gross ecosystem photosynthesis and respiration.

Acknowledgements

First author RW and senior author SRS designed the research. DDN, JBM, and MSZ designed and built the prototype QCLS instrument, and RW optimized the instrument for field measurements with contributions from SRS, SCW, DDN, JBM, and MSZ. RW conducted the research with advice from SRS, integrating with long-term Harvard Forest eddy flux data provided by JWM and SCW. RW wrote the paper together with SRS, with editorial contributions from all authors. This research was supported by the U.S. Department of Energy's Office of Science (BER), through both the Northeastern Regional Center of the National Institute for Climatic Change Research (award # 3594-UA-USDOE-4157) and the Terrestrial Ecosystem Science Program (award # DE-SC0006741).

Appendix A.

Here we present the equations used to convert back and forth between a set of CO_2 isotopologue molar mixing ratios $\{C^{626}, C^{636}, C^{826}\}$ and the corresponding set $\{C, \delta^{13}C, \delta^{18}O\}$. Three-digit superscripts denote molecules according to the old Air Force Geophysics Laboratory (AFGL) shorthand notation: "626" for $^{16}O^{12}C^{16}O$, "636" for $^{16}O^{13}C^{16}O$, and "826" for $^{18}O^{12}C^{16}O$. Two-digit superscripts continue to denote atoms, as in Section 2. We use the following values for the isotopic ratios of the Vienna Pee Dee Belemnite (VPDB) and Vienna Standard Mean Ocean Water (VSMOW) standards (Griffis et al., 2004; Baertschi, 1976; Allison et al., 1995; Li et al., 1988):

$$R_{\mathrm{VPDB}}^{13} = 0.0111797$$

$$R_{\mathrm{VSMOW}}^{18} = 0.0020052$$

$$R_{\mathrm{VSMOW}}^{17} = 0.0003799$$

Given the total molar mixing ratio C and the isotopic compositions $\delta^{13}C$ and $\delta^{18}O$, one can calculate the isotopologue molar mixing ratios C^{626}, C^{636}, and C^{826} as follows. First we convert the deltas to isotope ratios:

$$R^{13} = R_{\mathrm{VPDB}}^{13}(\delta^{13}\mathrm{C} + 1) \tag{A.1}$$

$$R^{18} = R_{\mathrm{VSMOW}}^{18}(\delta^{18}\mathrm{O} + 1) \tag{A.2}$$

$$R^{17} = R_{\mathrm{VSMOW}}^{17}(\delta^{18}\mathrm{O} + 1)^{0.516} \tag{A.3}$$

where we have used the relationship,

$$\frac{R^{17}}{R_{\mathrm{VSMOW}}^{17}} = \left(\frac{R^{18}}{R_{\mathrm{VSMOW}}^{18}}\right)^{0.516} \tag{A.4}$$

(Matsuhisa et al., 1978; Allison et al., 1995). We have no means to verify this relationship between ^{18}O and ^{17}O, but it is unlikely to be worse than simply assuming that $R^{17} = R_{\mathrm{VSMOW}}^{17}$, with respect to which Eq. (A.4) represents a correction of roughly 2.5%. A 2.5% error in R^{17} would correspond to about 1 in 10^5 oxygen atoms and lead to a 7 ppb error in the calculation of C^{626} when $C = 400$ ppm.

Next we find the fractions of the total carbon that are ^{12}C and ^{13}C:

$$f^{12} = \frac{1}{(1 + R^{13})} \tag{A.5}$$

$$f^{13} = R^{13} \cdot f^{12} \tag{A.6}$$

And we find the fractions of total oxygen that are ^{16}O, ^{18}O, and ^{17}O:

$$f^{16} = \frac{1}{(1 + R^{18} + R^{17})} \tag{A.7}$$

$$f^{18} = R^{18} \cdot f^{16} \tag{A.8}$$

$$f^{17} = R^{17} \cdot f^{16} \tag{A.9}$$

The isotopologue molar mixing ratios are then calculated as:

$$C^{626} = C \cdot f^{16} \cdot f^{12} \cdot f^{16} \tag{A.10}$$

$$C^{636} = C \cdot f^{16} \cdot f^{13} \cdot f^{16} \tag{A.11}$$

$$C^{826} = C \cdot 2 \cdot (f^{18} \cdot f^{12} \cdot f^{16}) \tag{A.12}$$

where we have assumed that the probability of a site in the molecule being occupied by a given isotope is equal to the relative abundance of that isotope, i.e. a given atom has no preference for bonding with one isotope over another. In reality, multiply substituted isotopologues, known as "clumps", are slightly favored thermodynamically (Eiler, 2007). Neglecting clumping, the carbon isotope flux ratio F_N^{13}/F_N^{12} is equal to the isotopologue flux ratio F_N^{636}/F_N^{626} while the oxygen isotope flux ratio F_N^{18}/F_N^{16} is equal to half the isotopologue flux ratio F_N^{826}/F_N^{626}, as there are two indistinguishable oxygen sites in the CO_2 molecule.

We now consider the reverse calculation. Given the isotopologue molar mixing ratios C^{626}, C^{636}, and C^{826}, one can find the total molar mixing ratio C and the isotopic compositions δ^{13}C and δ^{18}O as follows. For carbon, which appears only once in the molecule and has only two relevant isotopes (we neglect ^{14}C), the atomic isotopic composition is given by:

$$\delta^{13}C = \left(\frac{R^{13}}{R^{13}_{\mathrm{VPDB}}}\right) - 1; \quad R^{13} = \frac{C^{636}}{C^{626}} \tag{A.13}$$

For oxygen, which appears twice in the molecule, the atomic isotopic composition is given by:

$$\delta^{18}\mathrm{O} = \left(\frac{R^{18}}{R^{18}_{\mathrm{VSMOW}}}\right) - 1; \quad R^{18} = \frac{C^{826}}{(2C^{626})} \tag{A.14}$$

To calculate the total CO_2 molar mixing ratio, we need to determine the molar mixing ratios of the minor, unmeasured isotopologues. We start by calculating R^{17} from Eq. (A.3) and using Eqs. (A.5)–(A.9) to calculate f^{12}, f^{13}, etc. We then make the approximation $C \approx C_{\mathrm{guess}} = C^{626} + C^{636} + C^{826}$, which allows us to calculate the molar mixing ratios of the minor isotopologues involving ^{12}C as:

$$C^{726} = C \cdot 2 \cdot f^{17} \cdot f^{12} \cdot f^{16} \tag{A.15}$$

$$C^{827} = C \cdot 2 \cdot f^{18} \cdot f^{12} \cdot f^{17} \tag{A.16}$$

$$C^{828} = C \cdot f^{18} \cdot f^{12} \cdot f^{18} \tag{A.17}$$

$$C^{727} = C \cdot f^{17} \cdot f^{12} \cdot f^{17} \tag{A.18}$$

Finally, the total molar mixing ratio is obtained as:

$$\begin{aligned} C &= C^{626} + C^{826} + C^{726} + C^{828} + C^{827} + C^{727} + (C^{636} + C^{638} + C^{637} \\ &\quad + C^{838} + C^{837} + C^{737}) = (C^{626} + C^{826} + C^{726} + C^{828} + C^{827} \\ &\quad + C^{727}) \cdot (1 + C^{636}/C^{626}) \end{aligned} \tag{A.19}$$

References

Allison, C.E., Francey, R.J., Meijer, H.A.J., 1995. Recommendations for the Reporting of Stable Isotope Measurements of Carbon and Oxygen in CO_2 gas in Reference and Intercomparison Materials for Stable Isotopes of Light Elements (No. IAEA-TECDOC-825). International Atomic Energy Agency, pp. 155–162.

Baertschi, P., 1976. Absolute ^{18}O content of standard mean ocean water. Earth Planet. Sci. Lett. 31, 341–344.

Barford, C.C., Wofsy, S.C., Goulden, M.L., Munger, J.W., Pyle, E.H., Urbanski, S.P., Hutyra, L., Saleska, S.R., Fitzjarrald, D., Moore, K., 2001. Factors controlling long- and short-term sequestration of atmospheric CO_2 in a mid-latitude forest. Science 294, 1688–1691.

Bowling, D., Baldocchi, D., Monson, R., 1999. Dynamics of isotopic exchange of carbon dioxide in a Tennessee deciduous forest. Global Biogeochem. Cycles 13 (4), 903–922.

Bowling, D., Tans, P., Monson, R., 2001. Partitioning net ecosystem carbon exchange with isotopic fluxes of CO_2. Global Change Biol. 7, 127–145.

Eiler, J., 2007. Clumped-isotope geochemistry—the study of naturally-occurring, multiply-substituted isotopologues. Earth Planet. Sci. Lett. 262, 309–327.

Farquhar, G., Lloyd, J., Taylor, J., Flanagan, L., 1993. Vegetation effects on the isotope composition of oxygen in atmospheric CO_2. Nature 363, 439–443.

Farquhar, G.D., Ehleringer, J., Hubick, K.T., 1989. Carbon isotope discrimination and photosynthesis. Annu. Rev. Plant Physiol. Plant Mol. Biol. 40, 503–537.

Foken, T., 2006. 50 years of the Monin–Obukhov similarity theory. Boundary-Layer Meteorol. 119, 431–447.

Goulden, M., Munger, J., Fan, S., Daube, B., Wofsy, S., 1996. Measurements of carbon sequestration by long-term eddy covariance: methods and a critical evaluation of accuracy. Global Change Biol. 2, 169–182.

Griffis, T., Baker, J., Sargent, S., Tanner, B., Zhang, J., 2004. Measuring field-scale isotopic CO_2 fluxes with tunable diode laser absorption spectroscopy and micrometeorological techniques. Agric. For. Meteorol. 124, 15–29.

Griffis, T., Sargent, S., Baker, J., Lee, X., Tanner, B., Greene, J., Swiatek, E., Billmark, K., 2008. Direct measurement of biosphere-atmosphere isotopic CO_2 exchange using the eddy covariance technique. J. Geophys. Res. 113, D08304.

Howell, J., Mahrt, L., 1997. Multiresolution flux decomposition. Boundary-Layer Meteorol. 83, 117–137.

Knohl, A., Buchmann, N., 2005. Partitioning the net CO_2 flux of a deciduous forest into respiration and assimilation using stable carbon isotopes. Global Biogeochem. Cycles 19, GB4008.

Lai, C., Schauer, A., Owensby, C., Ham, J., 2003. Isotopic air sampling in a tallgrass prairie to partition net ecosystem CO_2 exchange. J. Geophys. Res. 108 (D18), 4566.

Lee, X., Massman, W., Law, B.E., 2004. Handbook of Micrometeorology: A Guide for Surface Flux Measurement and Analysis. Kluwer Academic Publishers, Dordrecht.

Lenschow, D., Raupach, M., 1991. The attenuation of fluctuations in scalar concentrations through sampling tubes. J. Geophys. Res. 96 (D8), 15259–15268.

Leuning, R., 2007. The correct form of the Webb, Pearman and Leuning equation for eddy fluxes of trace gases in steady and non-steady state, horizontally homogeneous flows. Boundary-Layer Meteorol. 123, 263–267.

Li, W.J., Ni, B.L., Jin, D.Q., Chang, T.L., 1988. Measurement of the absolute abundance of oxygen-17 in VSMOW. Kexue Tongbao (Chin. Sci. Bull.) 33, 1610–1613.

Matsuhisa, Y., Goldsmith, J.R., Clayton, R.N., 1978. Mechanisms of hydrothermal crystallization of quartz at 250 °C and 15 kbar. Geochim. Cosmochim. Acta 42, 173–182.

Mook, W., 2000. Environmental Isotopes in the Hydrological Cycle: Principles and Applications, vol. I: Introduction—Theory, Methods, Review. International Atomic Energy Agency.

Nelson, D., McManus, J., Herndon, S., Zahniser, M., Tuzson, B., Emmenegger, L., 2008. New method for isotopic ratio measurements of atmospheric carbon dioxide using a 4.3 μm pulsed quantum cascade laser. Appl. Phys. B 90, 301–309.

Ogée, J., Peylin, P., Ciais, P., Bariac, T., Brunet, Y., Berbigier, P., Roche, C., Richard, P., Bardoux, G., Bonnefond, J., 2003. Partitioning net ecosystem carbon exchange into net assimilation and respiration using $^{13}CO_2$ measurements: a cost-effective sampling strategy. Global Biogeochem. Cycles 17, 1070.

Ogée, J., Peylin, P., Cuntz, M., Bariac, T., Brunet, Y., Berbigier, P., Richard, P., Ciais, P., 2004. Partitioning net ecosystem carbon exchange into net assimilation and respiration with canopy-scale isotopic measurements: an error propagation analysis with $^{13}CO_2$ and $CO^{18}O$ data. Global Biogeochem. Cycles 18, GB2019.

Rothman, L.S., Gordon, I.E., Barbe, A., Benner, D.C., Bernath, P.F., Birk, M., Boudon, V., Brown, L.R., Campargue, A., Champion, J.P., Chance, K., Coudert, L.H., Dana, V., Devi, V.M., Fally, S., Flaud, J.M., Gamache, R.R., Goldman, A., Jacquemart, D., Kleiner, I., Lacome, N., Lafferty, W.J., Mandin, J.Y., Massie, S.T., Mikhailenko, S.N., Miller, C.E., Moazzen-Ahmadi, N., Naumenko, O.V., Nikitin, A.V., Orphal, J., Perevalov, V.I., Perrin, A., Predoi-Cross, A., Rinsland, C.P., Rotger, M., Šimečková, M., Smith, M.A.H., Sung, K., Tashkun, S.A., Tennyson, J., Toth, R.A., Vandaele, A.C., Vander Auwera, J., 2009. The HITRAN 2008 molecular spectroscopic database. J. Quant. Spectrosc. Radiat. Transfer 110, 533–572.

Saleska, S., Shorter, J., Herndon, S., Jiménez, R., McManus, J., Munger, J., Nelson, D., Zahniser, M., 2006. What are the instrumentation requirements for measuring the isotopic composition of net ecosystem exchange of CO_2 using eddy covariance methods? Isotopes Environ. Health Stud. 42, 115–133.

Sturm, P., Eugster, W., Knohl, A., 2012. Eddy covariance measurements of CO_2 isotopologues with a quantum cascade laser absorption spectrometer. Agric. For. Meteorol. 152, 73–82.

Tuzson, B., Mohn, J., Zeeman, M., Werner, R., Eugster, W., Zahniser, M., Nelson, D., McManus, J., Emmenegger, L., 2008. High precision and continuous field measurements of δ^{13}C and δ^{18}O in carbon dioxide with a cryogen-free QCLAS. Appl. Phys. B 92, 451–458.

Urbanski, S., Barford, C., Wofsy, S., Kucharik, C., Pyle, E., Budney, J., McKain, K., Fitzjarrald, D., Czikowsky, M., Munger, J., 2007. Factors controlling CO_2 exchange on timescales from hourly to decadal at Harvard Forest. J. Geophys. Res. 112, G02020.

Werle, P., Mucke, R., Slemr, F., 1993. The limits of signal averaging in atmospheric trace-gas monitoring by tunable diode-laser absorption spectroscopy (TDLAS). Appl. Phys. B 57, 131–139.

Wofsy, S., Goulden, M., Munger, J., Fan, S., Bakwin, P., Daube, B., Bassow, S., Bazzaz, F., 1993. Net exchange of CO_2 in a mid-latitude forest. Science 260, 1314–1317.

Yakir, D., Sternberg, L., 2000. The use of stable isotopes to study ecosystem gas exchange. Oecologia 123, 297–311.

Zobitz, J., Burns, S., Ogée, J., Reichstein, M., Bowling, D.R., 2007. Partitioning net ecosystem exchange of CO_2: a comparison of a Bayesian/isotope approach to environmental regression methods. J. Geophys. Res. 112, G03013.

Zobitz, J., Burns, S., Reichstein, M., Bowling, D.R., 2008. Partitioning net ecosystem carbon exchange and the carbon isotopic disequilibrium in a subalpine forest. Global Change Biol. 14, 1785–1800.